Materials Today Bio 32 (2025) 101766

Contents lists available at ScienceDirect

Materials Today Bio

journal homepage: www.journals.elsevier.com/materials-today-bio

3D-printed β-TCP scaffold as a bone-mimicking environment for an engineered model of osteosarcoma: *In vitro* properties and transcriptomic insights

Ksenia Menshikh [a], Virginia Alessandra Gobbo [b], Mauro Nascimben [a], Markus Hannula [b], Andrea Cochis [a], Tiziano Serra [c], Jonathan Massera [b,**], Abhay Pandit [d], Lia Rimondini [a,*]

[a] *Center for Translational Research on Autoimmune and Allergic Disease—CAAD, Department of Health Sciences, Università del Piemonte Orientale, 28100, Novara, Italy*
[b] *Faculty of Medicine and Health Technology, Tampere University, 33720, Tampere, Finland*
[c] *AO Research Institute Davos, 7270, Davos, Switzerland*
[d] *CÚRAM Research Ireland Centre for Medical Devices, University of Galway, Biomedical Sciences Building, Newcastle Road, Galway, H91 W2TY, Ireland*

ARTICLE INFO

Keywords:
Bone cancer
Tricalcium phosphate
Tumour engineering
In vitro 3D modelling
3D printing
3D porous scaffold

ABSTRACT

In the face of advancements in osteosarcoma research, existing preclinical models – including *in vitro* (i.e., two- and three-dimensional cell cultures, organoids) and *in vivo* approaches (i.e., xenografts, animal models) – are often characterised by low translatability, limiting their predictive power for clinical outcomes. This study investigated the potential use of a 3D-printed β-tricalcium phosphate (β-TCP) scaffold as a bone-mimicking environment in an advanced *in vitro* osteosarcoma preclinical model. The compatibility of the scaffold with osteosarcoma cell spheroids, endothelial cells, and primary bone marrow-derived mesenchymal stem cells (pBMSCs) was evaluated along with its physicochemical characteristics. Transcriptomic analysis of pBMSCs on the scaffolds revealed gene expression profiles indicating pronounced extracellular matrix organisation and minor osteogenic activity. The model effectively replicated significant aspects of the tumour microenvironment in a tri-culture system, with dynamic perfusion enhancing metabolic activity. The developed scaffold-based model was employed in the doxorubicin cytotoxicity test. The physiological significance of the tri-culture was demonstrated by its distinct doxorubicin accumulation, in contrast to spheroid monocultures. Despite the limitations of the proposed approach regarding efficient vascularisation of the model, this study highlights the potential of 3D-printed β-TCP scaffolds in tumour modelling to support physiologically relevant preclinical models.

1. Introduction

Nine of the ten tested drugs fail at the clinical trial stage [1]. One of the potential reasons for such a significant failure rate may be attributed to the drug discovery pipeline; test systems utilised in most preclinical investigations either lack complexity (conventional cell monolayer *in vitro* models) or translatability (*in vivo* models, i.e. experimental animals). The development of drugs that target osteosarcoma, the most common primary bone cancer, is not an exception. Patient survival rate has remained stagnant over the last 50 years [2]. A possible alternative to bridge the gap between preclinical and clinical testing is the utilisation of advanced *in vitro* tumour models that recapitulate the features of the microenvironment *in vivo*. Such models not only possess the potential for application in precision medicine, but also adhere to 3R (Replacement, Refinement and Reduction) requirements [3]. One of the shortcomings frequently met among modern 3D *in vitro* models of osteosarcoma is a lack of a bone-mimicking environment providing stimuli necessary for a tumour-like behaviour of the cancer cells [4,5]. In our study, we propose an approach to construct an *in vitro* osteosarcoma model that can simulate the complexity of bone cancer, enabling a more

---

[*] Corresponding author. Center for Translational Research on Autoimmune and Allergic Disease—CAAD, Department of Health Sciences, Università del Piemonte Orientale, 28100, Novara, Italy.

[**] Corresponding author. Faculty of Medicine and Health Technology, Tampere University, Korkeakoulunkatu 3, SM424, Tampere, 33720, Finland.

E-mail addresses: jonathan.massera@tuni.fi (J. Massera), lia.rimondini@med.uniupo.it (L. Rimondini).

https://doi.org/10.1016/j.mtbio.2025.101766
Received 19 February 2025; Received in revised form 1 April 2025; Accepted 11 April 2025

comprehensive investigation of the disease and subsequent evaluation of potential therapeutics.

In tumour engineering, a top-down approach is frequently employed, and the constituent elements of future *in vitro* models are delineated by deconstructing the *in vivo* entity into its essential components. In the case of osteosarcoma, which is hypothesised to originate from the bone marrow, the objective is to create a tumour-like unit (osteosarcoma cell spheroid) arranged within a bone-like environment (synthetic biomaterial scaffold), incorporating a source of vascularisation (endothelial cells) and external mechanical stimuli (perfusion bioreactor). This study focused on investigating the potential of a 3D-printed β-tricalcium phosphate (β-TCP) scaffold to serve as a bone-like environment for an advanced 3D *in vitro* model of osteosarcoma. Owing to its availability, osteoinductive, and osteoconductive properties, β-TCP is one of the most widely utilised calcium phosphates in the field of biomaterials for bone tissue engineering [6]. Numerous processing methods have been developed for fabricating biomaterial scaffolds for bone tissue engineering. Since the 2010s, interest in 3D printing has steadily increased, as evidenced by web search trends, particularly in the biomedical field. When coupled with the subsequent sintering step, 3D printing with β-TCP facilitates the creation of a controlled hierarchical structure with micropores and macropores, enabling enhanced cell attachment and proliferation [7]. Consequently, a 3D-printed β-TCP scaffold was selected as the candidate bone-mimicking compartment for the proposed bone cancer model.

The present work characterises the 3D-printed β-TCP scaffold from the perspectives of its chemical, structural, and mechanical properties, as well as its *in-vitro* performance in direct contact with cells and cell cocultures under both standard and perfusion conditions. Considering the desired application of the scaffold, we perform an in-depth study of gene expression in primary bone marrow-derived mesenchymal stem cells (pBMSCs) cultured on the β-TCP scaffold via transcriptomics analysis. We further utilise the cell-seeded scaffold to serve as a bone-like environment for osteosarcoma cell spheroids and demonstrate the application of the resulting model of osteosarcoma in a cytotoxicity assay of the well-known and widely used anticancer drug doxorubicin to its suitability as a physiologically relevant preclinical platform.

2. Materials and methods

2.1. Scaffold production

The scaffolds were produced by 3D printing β-TCP powder (Beta Tricalcium Phosphate, Whitlockite, Plasma Group Science®, UK; Batch P334S; mean diameter = 0.443 nm) using Pluronic® (F-127, Sigma-Aldrich, USA) as a sacrificial binder. The binder was prepared by mixing Pluronic® in ultrapure water (30 % wt/wt) for ~7 h using a magnetic stirrer and keeping the mixture on ice to prevent its solidification until a single homogeneous phase was obtained, referred to as pl30. To prepare the ink, β-TCP and pl30 were mixed at a 32/68 wt ratio. The mixture was vortexed at 2500 rpm for ~30 s and cooled on ice for ~30 s, repeatedly for approximately six cycles, until the ink was homogeneous and did not show any visible bubbles. The ink was collected using a syringe, transferred to an Optimum® 3 cc printing cartridge (Nordson EFD, Bedfordshire, UK), and left to stabilize for 20 min at room temperature (RT). 3Dn Tabletop Printer (nScrypt Inc., Orlando, Florida, USA), controlled via Machine Tool 3.0, was used for robocasting the scaffolds. The cartridge was attached to the 3D printer, and a SmoothFlow Tapered Tip (tip diameter Ø = 0.41 mm; Nordson EFD Optimum® SmoothFlow™, Westlake, Ohio, USA) was applied to the cartridge. The material feed was set to ~15.0–25.0 psi to guarantee a continuous and homogeneous flow, and the ink was extruded onto an acrylic sheet (Folex AG, Seewen, CH) using a script in .txt format. The shape of the scaffold was cylindrical, with a height of 8 mm and a diameter of 10 mm. The printed scaffolds were left overnight in a drying oven at 37 °C to stabilize the structure. After successive days, the scaffolds were sintered to fuse the β-TCP particles and remove the sacrificial pl30 as follows. The temperature was raised from room temperature (RT) to 500 °C at a rate of 1 °C/min. The samples were left to dwell at 500 °C for 1 h. Subsequently, the temperature was increased to 1150 °C at a rate of 5 °C/min. The samples were left to dwell at 1150 °C for 3 h. Subsequently, the temperature was reduced to 500 °C at a rate of 5 °C/min. Finally, the scaffolds were allowed to cool freely from 500 °C to room temperature (furnace inertia). The scaffolds were extracted from the furnace once the temperature was below 40 °C and stored in a desiccator for up to one month until analysis.

2.2. Scaffold physicochemical characterisation

A thorough physicochemical characterisation of the 3D-printed β-TCP scaffold was performed prior to its use in *in vitro* experiments. This analysis aimed to evaluate the scaffold's structural, compositional, and mechanical properties, which are critical for supporting cell attachment, proliferation, and extracellular matrix deposition.

2.2.1. Fourier-transform infrared spectroscopy

To confirm the β-TCP chemical structure post-scaffold production, Fourier-transform infrared (FTIR) spectroscopy was performed in the attenuated total reflection (ATR) mode (PerkinElmer Spectrum One FTIR Spectrophotometer (PerkinElmer, Waltham, MA)). For this, the scaffolds were milled to powder after sintering, and FTIR-ATR spectra were acquired within the wavenumber range of 4000-600 cm^{-1}, setting the resolution at 2 cm^{-1}, with each spectrum obtained by averaging 32 scans. As a control, spectra of the printed scaffold before sintering (β-TCP + pl30) were acquired. All the spectra were background-corrected and normalised to the band with the highest intensity.

2.2.2. X-ray diffraction analysis

To confirm the β-TCP crystalline structure after sintering, X-ray diffraction (XRD) analysis was conducted (Empyrean; Malvern Panalytical, UK). The scaffolds were milled into a fine powder, and measurements were performed in the 2θ diffraction angle range of 10°–100° using a cobalt tube (Kα = 1.789 Å).

2.2.3. Morphological analysis

To evaluate their surface morphology and chemical composition, the 3D-printed β-TCP scaffolds were analysed using scanning electron microscopy (SEM) with an energy-dispersive X-ray (EDX) spectrometry (JSM-IT500; Jeol, Japan). To acquire images using SEM, a backscattered electron detector was used, and scanning was performed at 15.0 kV, 30 Pa, a working distance of 11.7 mm and a probe current of 65.0 pA. For EDX spectrometry, areas of 300 μm × 225 μm were acquired at a magnification of 500 × . The 3D features of the scaffolds were analysed by micro-computed tomography (μCT, MicroXCT-400; Carl Zeiss X-ray Microscopy, Inc., USA) using an 80 kV tube voltage. The images were acquired with a 0.4 × objective and visualised using Avizo software (Thermo Fischer Scientific, USA).

2.2.4. Mechanical properties assessment

To assess the mechanical properties of the scaffold, a nanoindentation analysis and a compression test were performed. For determining the microscale Young's modulus, the scaffolds were indented with a probe (stiffness of 176.6 N/m and tip radius of 9.0 μm) using a Piuma Nanoindenter (Optics11 Life, NL). Measurements were performed in demineralised water to minimise the attractive forces between the material and the tip. The obtained data were optimised using an indentation model in the relevant range using DataViewer Software (v2.5.7, Optics11 Life, NL). The compression test was performed to evaluate the macroscale Young's modulus of the scaffolds. The analysis was conducted in triplicate using Instron Electropuls® E1000 (Instron, UK) and Bluehill Universal® Software. The measurements were done until the complete failure of the scaffolds, at a 0.5 mm/min deformation speed, and using a 2 kN load cell.

2.3. Scaffold in vitro biological characterisation

The cytocompatibility of the 3D-printed β-TCP scaffold was assessed to determine its ability to support cell adhesion, viability, and proliferation. This preliminary evaluation focused on understanding how immortalised mesenchymal stem cells and osteosarcoma spheroids interact with the scaffold, ensuring its suitability for further biological studies. In this section, inductively coupled plasma optical emission spectrometry was also performed to determine the release of ions from the scaffold in contact with cells.

2.3.1. Cell culture and spheroid generation

Human bone marrow-derived stem cells (hBMSCs; hTERT-BMSC clone Y201, immortalised through hTERT lentiviral vectors [8]) were cultivated in low-glucose Dulbecco's modified Eagle's medium (DMEM; Sigma-Aldrich, USA) supplemented with 15 % foetal bovine serum (FBS; Sigma-Aldrich, USA) and 1 % penicillin-streptomycin (PS; Invitrogen, USA). Human osteosarcoma cells (U2OS; HTB96, American Type Culture Collection, Manassas, USA) were cultured in high-glucose DMEM supplemented with 10 % FBS and 1 % PS. All the cell lines were maintained at 37 °C in a humidified atmosphere containing 5 % CO_2. Before the experiments, cells were cultivated until 80–90 % confluence, detached using trypsin-EDTA (1X; Sigma-Aldrich, USA) solution, harvested, and used for experiments.

For spheroid generation, wells of a 48-well plate were first coated with 1.5 % agarose solution under sterile conditions and were kept at RT under UV exposure for 2 h. Then, 5.0×10^4 U2OS cells were seeded per well of an agarose-coated plate. Cells were incubated under standard conditions with a culture medium that was changed every 2 or 3 days. Spheroid self-aggregation was monitored using light microscopy.

2.3.2. Cytocompatibility evaluation

Before use in the cytocompatibility assay, the β-TCP scaffolds were sterilised by heating at 140 °C for 3 h and quickly washed in sterile phosphate-buffered saline (PBS). hBMSCs were trypsinised, suspended in a 1:1 mixture of medium and collagen (PureCol® EZ Gel, 5 mg/mL), and seeded on a β-TCP scaffold. In the case of U2OS, 1-week cell spheroids were gently collected from the 48-well plate by pipetting, immersed in the collagen-media mixture, and injected into each scaffold. After 3 h of collagen solidification, the scaffolds were transferred to clean wells of a 24-well plate, and 1.5 mL of the culture medium was added. The culture medium was changed every 2–3 days.

Cell metabolic activity was assessed using a resazurin reduction assay (AlamarBlue ™, HS Cell Viability Reagent; Invitrogen, USA). The assay was chosen due to its high sensitivity, non-cytotoxicity, and suitability for long-term monitoring. This water-soluble, non-fluorescent violet dye is reduced by metabolically active cells into resorufin, a pink and fluorescent compound, allowing quantitative analysis based on fluorescence intensity in the supernatant. The reagent was added to the samples in fresh culture medium, and the fluorescence was read after 2 h of incubation at 560/590 nm using a plate reader (Spark®, Tecan Trading AG, CH). The viability and morphology of the cells were assessed by fluorescence microscopy with live/dead staining (LIVE/DEAD™ Viability/Cytotoxicity Kit, Calcein AM and Ethidium homodimer-1, for mammalian cells, Invitrogen, USA). Imaging was performed with a fluorescence microscope equipped with a humidified chamber at 37 °C and 5 % CO_2 – THUNDER Imager Live Cell & 3D Assay (Leica, Japan). At the end of the incubation period, the cell-seeded scaffolds were fixed in paraformaldehyde (reagent grade, crystalline; Sigma-Aldrich, USA), dehydrated by exposing them to ethanol at increasing concentrations, and dried by immersing them in hexamethyldisilazane (HMDS, Alfa Aesar, Waltham, USA) overnight in open air. After gold sputtering (DII-29019SCTR Smart Coater, Jeol, Japan), the samples were analysed by SEM.

2.3.3. Inductively coupled plasma optical emission spectrometry

To better understand the biochemical environment of the cells when cultured on the β-TCP scaffolds, we analysed the culture media using inductively coupled plasma optical emission spectrometry (ICP-OES). The analysis was done at key points of the experiments from the pre-incubation of the scaffolds in media up to the final point of culture of the assembled osteosarcoma model described in 2.5 (3 weeks of culture in total). As the culture medium was changed, 1 mL of the medium was collected and kept at −20 °C upon analysis. Once all samples were collected, they underwent a freeze-thaw cycle, were diluted in 9 mL distilled water, and stored at 4 °C for at least 24 h before the analysis. The concentrations of calcium and phosphorus (the main components of β-TCP) and magnesium and potassium (critical ions in cell homeostasis) were quantified.

2.4. Scaffold as a bone-like environment

After obtaining an overview of the physicochemical and biological properties of the β-TCP scaffold *in vitro*, we performed a prolonged experiment with primary bone marrow-derived mesenchymal stem cells (pBMSCs). We were interested in evaluating the scaffold based on its potential to activate osteogenic differentiation of pBMSCs to better mimic the bone microenvironment in the developed osteosarcoma model.

2.4.1. Cell culture and cell seeding procedure

PBMSCs (RoosterBio, USA) were first expanded in the specialised xeno-free expansion media RoosterNourish™ (RoosterBio, USA), and then cultivated in Minimum Essential Medium α (α-MEM, GlutaMAX™ Supplement; Gibco, USA) supplemented with 10 % FBS, 1 % PS, and 10 ng/mL of human heat-stable bFGF Recombinant Protein (FGF2, Gibco, USA) and maintained at 37 °C in a humidified atmosphere containing 5 % CO_2. The seeding procedure was performed as previously described. Briefly, β-TCP scaffolds were kept at 140 °C for 3 h, washed in sterile PBS, and immersed overnight in FBS-enriched culture medium. PBMSCs were trypsinised, suspended in a 1:1 mixture of medium and 5 mg/mL collagen, and seeded on β-TCP scaffolds at a number of 3.0×10^5 cells per scaffold. After 3 h of collagen solidification, the scaffolds were transferred to a 24-well plate, and 1.5 mL of culture medium without FGF2 was added. The cell-seeded scaffolds were monitored using metabolic activity (resazurin reduction) and viability (live/dead fluorescent staining) assays as described above in 2.3.2.

As positive and negative controls of osteogenic differentiation, the cells were also seeded in the wells of a 24-well plate as monolayers and cultured either in a standard culture medium without FGF2 or in an osteogenic medium containing low-glucose DMEM supplemented with 10 % FBS, 1 % PS, 20 mM β-glycerophosphate (disodium salt hydrate, BioUltra, ≥99 % (titration)), 50 μM L-ascorbic acid 2-phosphate (sesquimagnesium salt hydrate, ≥95 %), and 10^{-7} M dexamethasone (≥97 %; all – Sigma-Aldrich, USA).

2.4.2. Alkaline phosphatase activity assay

Increased alkaline phosphatase (ALP) activity is an early marker of osteogenic differentiation. To evaluate its intracellular level, the assay was performed on the protein extracted from pBMSCs cultured on the scaffolds. The total protein was recovered from the flow-through obtained during RNA extraction (see 2.4.3) using the acetone precipitation method: cold acetone was added in a volume four times that of the flow-through sample, the mix was briefly vortexed, incubated at −20 °C for 1 h, and centrifuged for 10 min at 15000×*g*. The pellet was dried and resuspended in the buffer provided in the ALP assay kit (Alkaline Phosphatase Assay Kit, Colorimetric, Abcam, UK). The activity of ALP in the extracted protein was determined following the protocol recommended by the manufacturer. The obtained values were normalised to the total protein amount estimated using the Coomassie (Bradford) assay following the manufacturer's instructions (Protein Assay Dye

Reagent Concentrate; Bio-Rad, USA).

2.4.3. mRNA-Seq and differential gene expression analysis

For mRNA-Seq analysis, RNA was extracted from the samples. For this, the cell-seeded scaffolds were disrupted by thorough vortexing in 2-mL tubes with tungsten carbide beads (Qiagen, Germany) in lysis buffer (Qiagen, Germany), and then the recommended protocol of RNeasy Plus Mini Kit (Qiagen, Germany) was followed. The concentration (at least 10 ng/μL) and integrity (at least 4) of the extracted RNA were analysed using a spectrophotometer (NanoDrop 2000, Thermo Scientific, USA) and BioAnalyzer (Agilent RNA 6000 Nano, Agilent Technologies, USA), respectively. mRNA sequencing was performed by Novogene (Cambridge, UK) using the NovaSeq 6000 platform (Illumina, USA), with an S4 flow cell using the 300-cycle kit v1.5. The generated paired-end 150 bp reads were aligned to the Homo Sapiens (GRCh38/hg38) reference genome.

2.4.4. Transcriptomics data and statistics

Raw data (raw reads) in fastq format were first processed using in-house Perl scripts. In this step, clean data (clean reads) were obtained by removing reads containing adapters and reads containing poly-N and low quality; at the same time, Q20, Q30, and GC content were calculated. All downstream analyses were based on the cleaned data. Quantification of gene expression levels was performed using featureCounts v1.5.0-p3 to count the number of reads mapped to each gene. Differential expression analysis statistical analysis was carried out through the DESeq2 R package (1.20.0). DESeq2 provides statistical routines for determining differential expression in digital gene expression data using a model based on negative binomial distribution. The resulting P-values were adjusted using Benjamini and Hochberg's approach to control the false discovery rate. Prior to differential gene expression analysis, the read counts for each sequenced library were adjusted using the edgeR (3.22.5) program package through one scaling normalised factor.

2.4.5. Functional analysis

Gene expression levels were filtered by thresholding the fold-change and statistical values from the volcano plots to obtain lists of markedly modified genes to characterise the two experimental conditions. The ontology sources applied to perform enrichment analysis were the KEGG Pathway, GO Biological Processes, Reactome Gene Sets, Canonical Pathways, CORUM, WikiPathways, and PANTHER databases [9–13]. In addition, Metascape software has been used to synthesise and process information [14]. Every gene in the genome served as the backdrop for enrichment, and terms were grouped based on their membership similarities, considering a p-value <0.01, a minimum count of 3, and an enrichment factor >1.5 (the enrichment factor is the ratio between the observed counts and the counts expected by chance). Specifically, q-values were computed using the Benjamini-Hochberg process to adjust for multiple testing, while p-values were computed using the cumulative hypergeometric distribution. Sub-trees with a similarity of >0.3 are regarded as clusters when hierarchical clustering is applied to the enriched phrases using Cohen's kappa as the similarity metric. To summarise the information provided during clustering analysis and aid in identifying important biological bioactivities, a cluster could be represented by the statistically most significant term within it (for instance, the term with the lowest p-value).

2.5. Scaffold application in 3D in vitro model of osteosarcoma

Previously, we defined four possible "building blocks" of the *in vitro* model of osteosarcoma. In the preceding sections, we described one of them, a bone-like environment, represented by a pBMSC-seeded β-TCP scaffold. In the following sections, the assembly of the complete model is described. In Fig. 1, we present the scheme of this assembly up to the application of the model in a cytotoxicity assay of the anticancer drug doxorubicin.

2.5.1. Pre-culture of pBMSCs on the scaffolds and spheroid generation

PBMSCs were cultured and seeded onto sterilised and pre-incubated scaffolds as described in the previous sections. To estimate cell metabolic activity on the 1st day of culture, the scaffolds were transferred to a clean 24-well plate, and a resazurin reduction assay was performed, both in the plate used for cell seeding and the clean plate with newly transferred scaffolds. The metabolic activity of the pBMSCs on the scaffolds, as well as their viability, was also assessed on the 3rd and 6th days of culture by resazurin reduction assay and fluorescence microscopy with live/dead staining, as described above (2.3.2).

Spheroids were generated following the agarose-coated plate method described above (2.3.1). To optimise the mechanical stability of the spheroids and provide a more physiological-like microenvironment, U2OS cells were mixed with hBMSCs Y201 cells in a 3:1 ratio, and 5×10^5 cells were seeded per well of the agarose-coated plate. The cells were incubated in a 1:1 mixture of the relevant culture medium. The spheroid self-aggregation was monitored by light microscopy.

2.5.2. Endothelial cell culture and tri-culture assembling

Human dermal microvascular endothelial cell lines (TIME-GFP, CRL-4045, ATCC, USA) were cultured in Vascular Cell Basal Medium (ATCC, USA) with the addition of the Microvascular Endothelial Cell Growth Kit-BBE (ATCC, USA), 200 μg/mL G418 (G418 disulfate salt solution for cell culture; Sigma-Aldrich, USA) and 12.5 μg/mL Blasticidin (Blasticidin S HCl; Gibco, USA).

One day before assembling the tri-culture on the scaffolds, the U2OS-MSC spheroids were stained with DiD (Vybrant™ Multicolour Cell-Labelling Kit, Invitrogen, USA). On the day of tri-culture assembly, both co-culture spheroids and endothelial single-cell suspensions were seeded on the 7-day precultured pBMSC-seeded scaffolds in 100 μL of a collagen-medium mix. After 3 h of collagen solidification, 1.5 mL of a medium composed of a 1:1:1 mixture of media for pBMSCs, U2OS, and endothelial cells was added per scaffold. Scaffolds seeded with co-culture spheroids were used as a control and incubated in a 1:1 mix of media for U2OS and hBMSCs Y201. For the metabolic activity assay, the tri-culture scaffolds were transferred to a clean multiwell plate, and the resazurin reduction assay was performed as described above (2.3.2). For

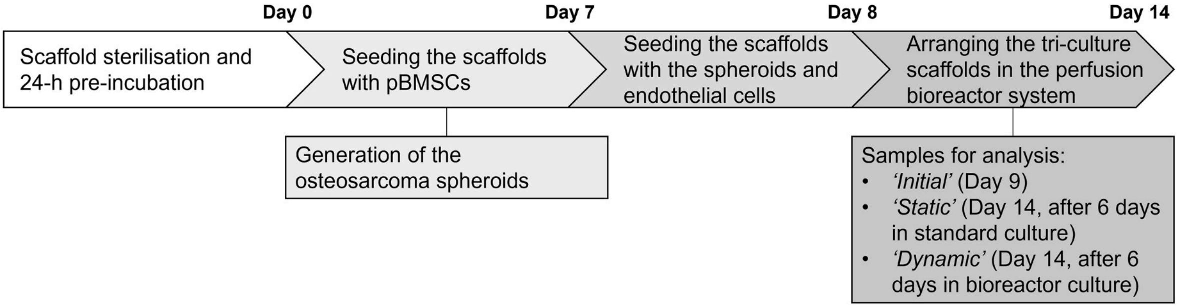

Fig. 1. – Scheme of the 3D *in vitro* osteosarcoma model assembly.

morphological analysis, the scaffolds were observed using fluorescence microscopy and Calcein AM staining to label live cells, acetylated LDL (Low-Density Lipoprotein from Human Plasma, Acetylated, Alexa Fluor™ 488 Conjugate, Invitrogen, USA) to label endothelial cells, and the above-mentioned DiD to label osteosarcoma spheroids.

2.5.3. Gene expression analysis in tri-culture

Total RNA was extracted from the samples (spheroid-seeded and tri-culture seeded scaffolds) as described above (2.4.3). The extracted RNA (500 μg) was used to synthesise cDNA (iScript™ cDNA Synthesis Kit, Bio-Rad Laboratories, USA). The gene expression level was analysed using a master mix for quantitative real-time PCR (SsoAdvanced Universal SYBR Green Supermix, Bio-Rad Laboratories, USA) with a reference to actin beta (ACTB), chosen as a normalisation gene. Primers were designed using PrimerQuest™ Tool and synthesised by Integrated DNA Technologies (IDT, USA). The sequences of forward and reverse primers are listed in Table S1. The values were related to the control by the $^{\Delta\Delta}$Ct method [15].

2.5.4. Scaffold vascularisation assay

To demonstrate the ability of the developed model of osteosarcoma to be vascularised, we carried out an endothelial cell migration assay that uncouples the impact of β-TCP from the impact of osteosarcoma spheroids on endothelial cell network formation. The scaffold volume may lead to inefficient oxygen and nutrient transport and subsequently affect vascularisation. To exclude this factor and focus on the possibility that the chemical structure of β-TCP rather than scaffold volume may impair the capillary-like endothelial cell formation, we used the milled scaffolds.

2.5.4.1. Milled β-TCP scaffold. The 3D-printed scaffolds were milled in a mortar with a pestle. SEM was performed to confirm the maintenance of the β-TCP granular morphology after milling. Briefly, the particles of the milled scaffolds were thinly spread on adhesive tape, gold-sputtered (DII-29019SCTR Smart Coater, Jeol, Japan), and analysed (JSM-IT500, Jeol, Japan).

2.5.4.2. Cell culture and spheroid formation. Red Fluorescent Protein-expressing Human Umbilical Vein Endothelial Cells (RFP-HUVECs; cAP-0001RFP, Angio-Proteomie, USA) were cultured in EBM™-2 Basal Medium (Lonza, CH) supplemented with EGM™-2 SingleQuots® Supplements (Lonza, CH) in pre-coated culture flasks (Quick Coating Solution, Angio-Proteomie, USA). GFP-expressing osteosarcoma cells MGreen63 (obtained previously via transducing with GFP-containing lentiviral vector MG63 cell line; European Collection of Cultured Cells, UK) were cultured in high-glucose DMEM supplemented with 1 % PS and 10 % FBS. All the cell lines were maintained at 37 °C in a humidified atmosphere containing 5 % CO_2. To form osteosarcoma cell spheroids, an AggreWell™ 400 plate (400 μm ø microwells, StemCell Technologies, Canada), precoated with AggreWell™ Rinsing Solution (StemCell Technologies, Canada), was used. To define the optimal cell concentration in terms of spheroid formation and ease of subsequent patterning, routinely harvested MGreen63 cells were seeded at 7.0×10^5, 1.4×10^6, and 3.5×10^6 cells per well of a 6-well AggreWell™ plate with the expectation of 100, 200, and 500 cells per spheroid, respectively, according to the manufacturer's recommendations. Spheroid formation was monitored using brightfield microscopy.

2.5.4.3. Endothelial cell migration assay. To assemble the patterning chamber, a sterile frame (poly(methyl methacrylate), inner ø 1 cm, 1 mm thick) was aseptically attached with double adhesive tape inside a 35 mm dish for imaging (μ-Dish 35 mm, high, ibidi GmbH, Germany). Sterilised and pre-incubated in FBS-rich medium, β-TCP particles (1 mg) obtained after the scaffold milling were resuspended in 80 μL fibrinogen (50–90 mg/mL, Evicel®) and poured into the centre of the frame. Using clamps, the dish was fixed on top of the sample holder attached to a mechanical driver. By controlling the actuator, the driver was set to vertical vibrations at a frequency of 70 Hz. After patterning the particles in a ring shape, 25 μL of human thrombin (800–1200 UI/mL) was added on top of the fibrinogen disk with the patterned particles. The chamber was left in an incubator for 30 min for solidification. For osteosarcoma spheroid patterning, the same procedure was followed, with the harvested spheroids used instead of β-TCP particles. After fibrin formation, endothelial cells were seeded as a single-cell suspension in medium (1.5×10^5 cells in 150 μL) on top of the fibrin gel. The cell-seeded construct was kept in the incubator for 2 h to allow cells to settle and attach to fibrin. The culture medium was filled to 3 mL per chamber and changed every 2 days until the end of the experiment (5 days).

2.5.4.4. Imaging. On the day of patterning, as well as after 24 and 48 h of culture, the samples were analysed using a Zeiss LSM800 confocal microscope equipped with a CCD camera (Axiocam 506 colour). On the 5th day, the samples were fixed in 4 % paraformaldehyde for 2 h at RT, washed in PBS three times, and kept in PBS at 4 °C. For immunostaining, the samples were permeabilised in 2 % triton X-100 for 1 h, RT, non-specific sites were blocked with 4 % BSA solution in PBS for 2 h, RT, and PECAM-1 (1:100 in PBS, Anti-Hu CD31 Alexa Fluor™ 488-conjugated; Invitrogen, USA) was kept overnight at 4 °C. Before imaging, samples were counterstained with Hoechst 33342 (Thermo Scientific, USA) for 10 min. The samples were then analysed using a THUNDER Imager Live Cell & 3D Assay (Leica, Japan).

From the obtained Z-stacks, the maximum intensity Z-projections of the images were generated using the ImageJ software (NIH, USA) and used for the following analysis. From the sample 5 × overview images, the Radial Profile signal was extracted to analyse the colocalization of the endothelial cell network and patterned osteosarcoma spheroids and/or scaffold particles. Detailed 20 × images were used to analyse the expression of tight junction protein PECAM-1 in the formed endothelial cell network.

2.6. Application of tri-culture model in cytotoxicity test

To preliminarily evaluate the performance of the tri-culture model in anticancer drug cytotoxicity applications, doxorubicin (DOX) was added to the culture medium of scaffolds cultured for 6 days under static and dynamic conditions. In the case of the dynamic system, an additional reservoir bottle was added, and the chambers were divided into two separate sequences: one connected to a reservoir with regular culture medium, and another connected to a reservoir with medium containing DOX, as shown in Fig. S1. After 24 h, DOX accumulation was analysed via fluorescent microscopy of the tri-culture scaffolds incubated under static and dynamic conditions with or without the tested anticancer drug. Spheroid-seeded scaffolds cultured under static conditions were used as controls.

2.7. Statistical analysis

In the analyses, each group of samples was represented by three replicates. The statistical analysis and data representation approach in the context of transcriptomic analysis was described in the relevant sections (2.4.5 and 2.4.6). For other quantification analyses, the results are presented as the mean value ± standard deviation. Comparisons between groups within experimental time points were performed in Prism (v8, GraphPad Software, USA) using one-way ANOVA with Tukey's correction for multiple comparisons, preceded by normal distribution Shapiro–Wilk's and homoscedasticity Levene's median tests. For each comparison, differences were considered significant at $p < 0.05$. To filter the quantity of information during specific analyses, lower thresholds can be implemented and subsequently reported.

3. Results

3.1. Scaffold physicochemical characterisation

The physicochemical properties of the 3D-printed β-TCP scaffold were analysed to evaluate its structural, compositional, and mechanical characteristics. These properties are essential for ensuring the scaffold's suitability as a bone-mimicking environment and its ability to support cellular interactions in the *in vitro* osteosarcoma model.

3.1.1. Fourier-transform infrared spectroscopy and X-ray powder diffraction analysis

FTIR-ATR spectroscopy was used to assess changes in the surface chemical structure of the scaffolds before and after sintering (Fig. 2, a). Before sintering, the presence of Pluronic® F127 is confirmed by its characteristic peaks and bands [16–18]: 2980 cm^{-1} corresponds to OH vibration, 2880 cm^{-1} – to CH stretching, 1369 cm^{-1} – to CH$_3$, 1341 cm^{-1} – to CH$_2$ (wagging), 1282 and 1241 cm^{-1} – to CH$_2$ (twisting); 1098, 1053, and 1016 cm^{-1} – to C-O-C (stretching); while the peak at 956 and the shoulder at 938 cm^{-1} are assigned to CH$_2$ (rocking). The peaks at 997 and 924 cm^{-1} correspond to HPO$_4^{2-}$, and the peak at 745 cm^{-1} is attributed to P-O-P stretching [19,20] confirming the presence of β-TCP powder dispersed in the pluronic (pl30) matrix. The hydrogenation of the phosphate group was explained by the strong hydration of the system, due to the high content of water in the continuous pl30 matrix.

After sintering, the peak at 745 cm^{-1}, attributed to P-O-P stretching, was maintained. High-intensity bands were also detected at 1121, 1083, 1045, 973 and 946 cm^{-1}, attributed to the stretching of the tetrahedral [PO$_4$]$^{3-}$ groups [19,20]. Post sintering, all peaks assigned to the pl30 matrix disappear, including water vibrations, confirming the complete decomposition and evaporation of the pluronic.

XRD analysis was performed to assess eventual variations in the crystalline structure of β-TCP after sintering (Fig. 2, b). The spectra of β-TCP, before and after sintering, were characterised by the same peaks, matching with the theoretical whitlockite pattern (ICDD 00-009-0169, Fig. 2, b) [21]. This was explained as the original stock powder contains a relatively high percentage of magnesium (up to 2500 ppm) and it is constituted by both β-TCP and whitlockite phases. Moreover, a mild shift to the right (higher 2θ values) of all the peaks was observed after the sintering process, towards the position of β-TCP peaks (ICDD 00-003-0713, Fig. 2, b) [22,23]. The narrower diffraction peaks after sintering were attributed to a higher β-TCP crystallization and the increase in the crystal dimensions [24]. Overall, these observations suggested a partial phase transformation from whitlockite to β-TCP, which needs deeper future studies to be fully confirmed.

3.1.2. Morphological and mechanical analysis

The 2D and 3D features of the scaffolds are shown in Fig. 3, a and b and c. The scaffolds were characterised by lattice struts with an average width of 372.83 ± 40.44 μm. The pore sizes were, on average, 264 ± 24 μm, 257 ± 34 μm, and 170.95 ± 32.92 μm, in x, y and z directions, respectively. The overall porosity was assessed to be 40 ± 7 %. At the microscale, the material was composed of granules with diameters varying between 6.03 and 31.13 μm and with inter- and intragranular porosity. The average diameter of the granules remained stable with time of immersing in media (15.67 ± 7.2 μm, 15.99 ± 6.07 μm, and 16.83 ± 5.67 μm for intact scaffold, scaffold incubated in media for 3 days and 7 days, respectively). The distribution of elements on the surface of the intact scaffold and the elemental composition throughout different incubation periods (3 days and 7 days in medium) were shown by standardless EDX analysis and are presented in Fig. 3, d. The results for each time point are shown in Fig. S2. As for the stiffness analysis, owing to the high intragranular porosity, circular cross-section of the scaffold struts, and peculiarities of the nanoindentation process, a wide range of effective Young's modulus values was determined. The distribution of the values obtained by indenting a 10 μm × 10 μm matrix of the strut is shown in Fig. 3, e. The values were divided into three distinct groups: the majority of the indented points resulted in the average E (eff) = 66.46 ± 29.26 MPa, and two other smaller groups reached the average of 274.75 ± 114.27 MPa and 1412.5 ± 509.75 MPa. The macroscale Young's modulus obtained in the compression test was measured at 11.17 ± 2.90 MPa.

In this section, the structural, compositional, and mechanical properties of the 3D-printed β-TCP scaffold were analysed to determine the potential impact of these properties on cell behavior and scaffold performance in the *in vitro* model.

3.2. Scaffold in vitro biological characterisation

The *in vitro* characterisation of the 3D-printed β-TCP scaffold was performed to assess its cytocompatibility with different cell types. This evaluation focused on cell adhesion, viability, and metabolic activity, providing insights into the scaffold's ability to serve as an engineered environment for the developed model.

The scaffold cytocompatibility assessment showed different trends in the metabolic activity of hBMSCs and U2OS spheroids cultivated on printed β-TCP scaffolds (Fig. 4, a). Owing to a higher total cell count, on the first day of cultivation, hBMSCs demonstrated higher relative fluorescent unit (RFU) values than U2OS cell spheroids. This difference was

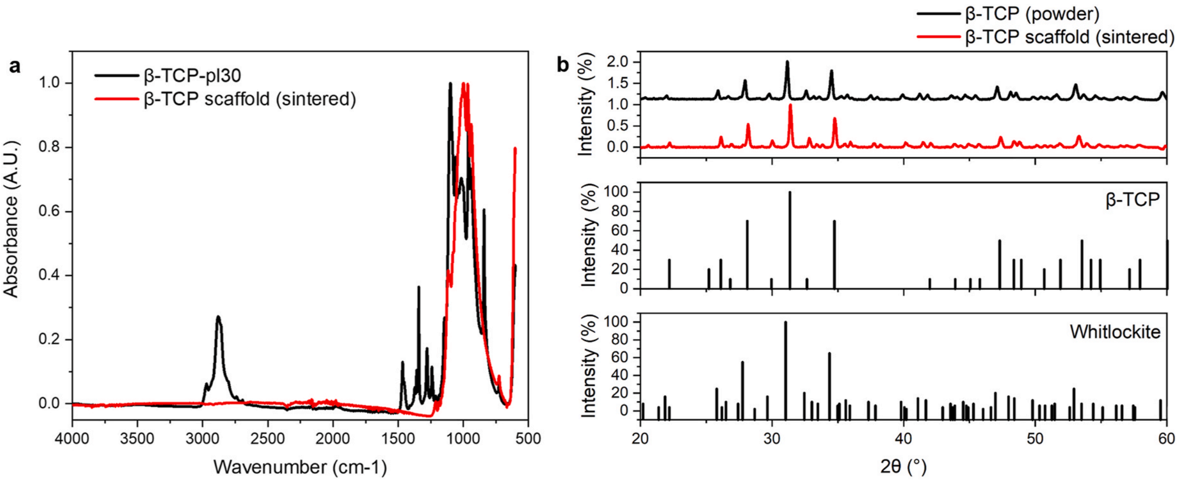

Fig. 2. – FTIR-ATR spectroscopy (a) of β-TCP scaffolds before (black line) and after (red line) sintering. XRD analysis (b) of β-TCP scaffolds after sintering. (For interpretation of the references to colour in this figure legend, the reader is referred to the Web version of this article.)

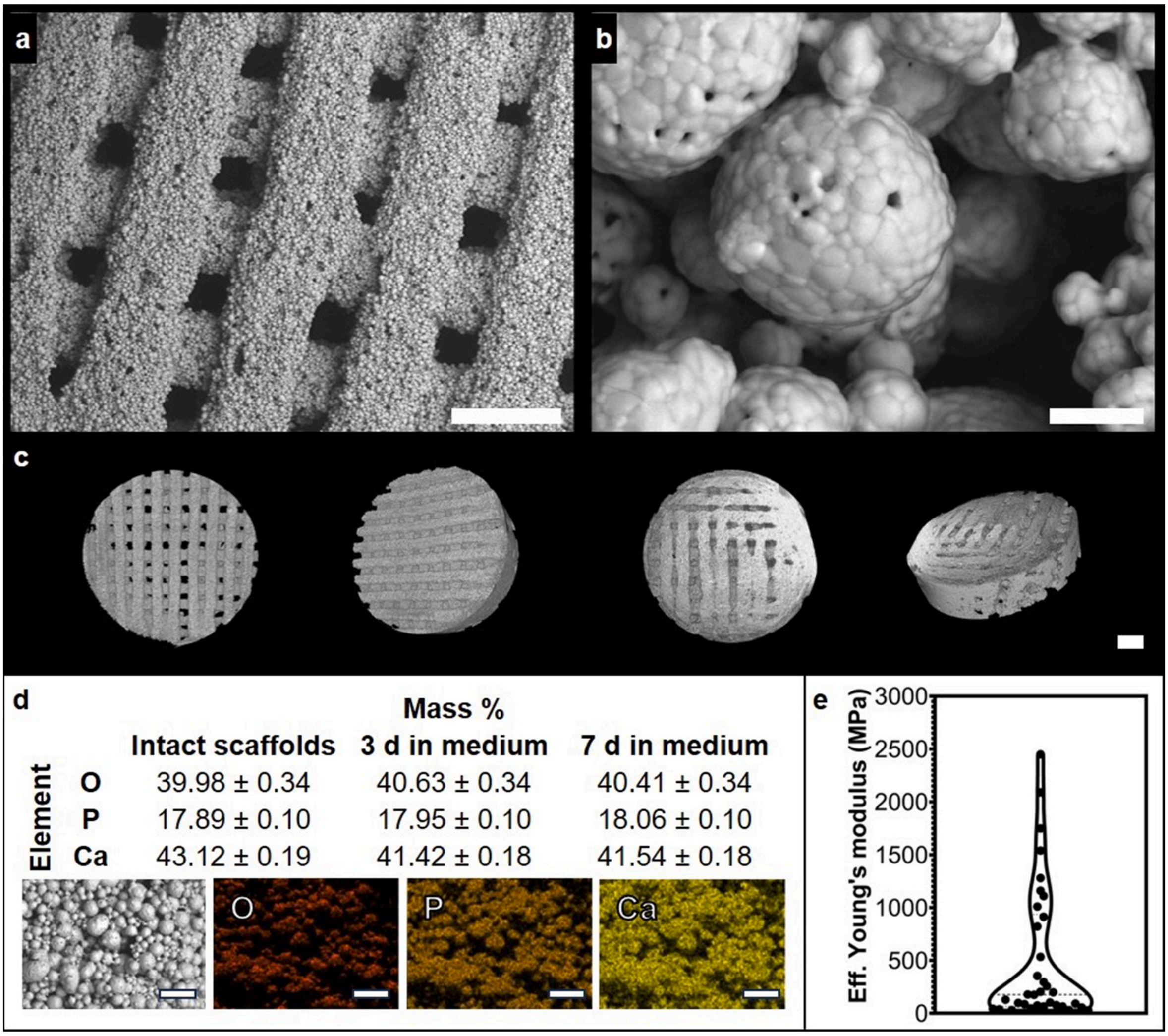

Element	Intact scaffolds	3 d in medium	7 d in medium
O	39.98 ± 0.34	40.63 ± 0.34	40.41 ± 0.34
P	17.89 ± 0.10	17.95 ± 0.10	18.06 ± 0.10
Ca	43.12 ± 0.19	41.42 ± 0.18	41.54 ± 0.18

Fig. 3. – a, b and c: Microstructure of the 3D-printed β-TCP scaffolds defined by SEM (a and b) and μCT (c). Scale bars: 500 μm (a), 10 μm (b) and 1000 μm (c). d: Element mapping and standardless EDX analysis of the intact β-TCP scaffold and scaffolds incubated in culture medium for 3 and 7 days; the values are reported as relative intensities of the identified peaks normalised to 100 % ± measurement error; scale bars 50 μm. e: distribution of stiffness values obtained for one strut of the scaffold.

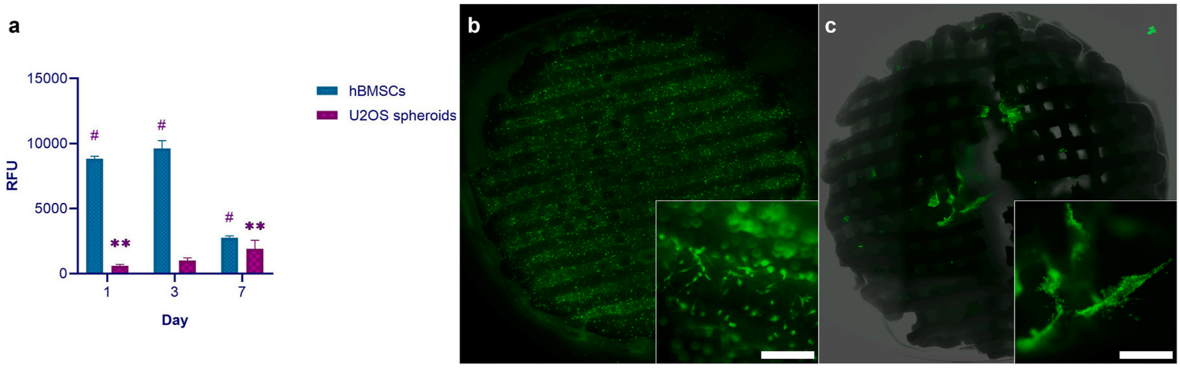

Fig. 4. – a: Metabolic activity of U2OS cell spheroids and hBMSCs cultivated on printed β-TCP scaffolds. Values are presented as the mean ± SD of the relative fluorescent units (RFU), n = 3. Multiple comparisons were performed using two-way ANOVA with Tukey's correction; ** – significant differences between groups of samples, $p < 0.01$, # – $p < 0.0001$. b and c: Fluorescent microscopy images of viable hBMSCs cells (b) and U2OS cell spheroids (c) seeded on the 3D-printed β-TCP scaffolds. Calcein AM staining; scale bar 200 μm.

maintained on the 3rd day. However, the viability of hBMSCs after 1 week decreased significantly compared to that at previous time points and equalised to that of U2OS cells. In contrast, osteosarcoma cell spheroids showed significantly higher metabolic activity on the 7th day compared to that on the 1st day of the test.

Calcein AM staining performed on the 7th day of hBMSC culture on β-TCP scaffolds showed an even spread of the cells throughout the sample volume (Fig. 4, b). The hBMSCs cells mostly covered the surface of the scaffold and had an elongated shape. U2OS cell spheroids at the same time point were arranged in the centre of the scaffold, partly covering the scaffold's surface and partly supported by collagen or extracellular matrix (Fig. 4, c).

3.3. *Scaffold as a bone-like environment*

To evaluate the ability of the 3D-printed β-TCP scaffold to serve as a bone-like environment, primary bone marrow-derived mesenchymal stem cells (pBMSCs) were cultured on the scaffold for an extended period. The study focused on assessing cell metabolic activity, extracellular matrix (ECM) synthesis, and potential osteogenic differentiation.

3.3.1. *Cell metabolic activity, viability and morphology*

The metabolic activity of the pBMSCs seeded on the scaffolds was maintained after 3 weeks of cultivation (Fig. S3). The viability of the cells on the scaffolds was confirmed by fluorescent microscopy observation with Calcein AM staining on the 3rd and the 6th days of culture (Fig. 5a and b). In comparison to the earlier time points, cells on the images at the later time points were more oriented and elongated. Moreover, in the areas between the scaffold structures, neighbouring struts, small gaps, or sharp corners, the cells produced a more organised and abundant ECM. For SEM imaging, the scaffolds cultured for three weeks were cut perpendicular to the z-axis of the printing. Along with live observations, dense cell sheets were found to cover the surface of the material, and the intergranular space of β-TCP was rich in the newly synthesised ECM (Fig. 5, c).

3.3.2. *Alkaline phosphatase activity*

Increased ALP activity is an early marker of osteogenic differentiation. To assess its intracellular levels, pBMSCs cultured on β-TCP scaffolds were lysed, and the obtained values of ALP activity were normalised to the total protein concentration. Compared to the initial point (3 d), there was a significant increase in ALP activity on the 10th day of culture, with a following slight decrease (Fig. S4).

3.3.3. *Transcriptomic analysis*

Transcriptomic data analysis was performed on the RNA extracted from pBMSCs cultured for 3 weeks on β-TCP scaffolds in regular medium (T) to evaluate differential gene expression in comparison with pBMSCs cultured for 3 weeks under standard conditions (as a monolayer) in regular medium (R) or osteogenic differentiation medium (B). Additional analysis tracked the evolution of the gene profiles during the experimental time course (from day 3 to day 21).

3.3.3.1. Highly regulated genes on scaffolds and in osteogenic medium. Volcano plots comparing the two experimental conditions, T (scaffolds) and B (osteogenic medium), were filtered to define subsets of genes belonging to specific regions of interest through custom Python scripts by applying thresholds of $p = 0.01$ and log2 fold change of 4 (thick dash-dotted lines in the related figures). As a reference, canonical thresholds of $p = 0.05$ and log2 fold change of 2 were marked with the same line types but with a finer stroke. The regions of interest defined by the thresholds are shaded in grey, and genes falling inside these areas of the volcano plots are coloured in accordance with the similarities in up- or downregulation between groups, following the colour scheme reported in Table S2. As an example, Fig. 6 illustrates the volcano plots and colours applied to upregulated genes in both T (scaffolds) and B (osteogenic medium) conditions compared to R (regular medium). Inside the region of interest, genes markedly and positively co-regulated ($\log F.C. > 4$ and $p < 0.01$ on both T and B) are shown in green, whereas genes extremely upregulated on T ($\log F.C. > 4$ on T and $\log F.C. < 2$ on B) are shown in red. Similarly, genes exclusively upregulated on B ($\log F.C. > 4$ on B and $\log F.C. < 2$ on T) were violet, while genes mildly regulated in one condition ($\log F.C. > 4$ on T and $2 > \log F.C. > 4$ on B) and extremely regulated in the other ($\log F.C. > 4$ on B and $2 > \log F.C. > 4$ on T) were coloured in blue or teal. The other subsets of genes are illustrated in volcano plots in Figs. S5–S7.

The analysis paid special attention to gene lists that could help characterise one experimental condition by highlighting associated biological processes or gene ontology terms. The most relevant enriched terms from the gene lists enclosing those extremely up- or downregulated for T or B only (equivalent to genes reported in red or violet on the volcano plots) are shown in Fig. 7, and the heatmap containing the full list of enriched terms is in Fig. S8. The figure reports the largest clusters represented by the most significantly enriched terms and related p-values; as an example, the term "Naba matrisome associated" (ensemble of genes encoding ECM-associated proteins including ECM-affiliated proteins, ECM regulators, and secreted factors) is statistically relevant and shared across experimental conditions. The genes markedly upregulated only in condition T were significantly involved in VEGFA/VEGFR2 signalling and glycolysis, whereas genes found to be extremely downregulated in condition T included the regulation of angiogenesis and oxidative stress. In condition B, extremely downregulated genes were related to tissue morphogenesis, vasculature development, DNA transcription, and extracellular matrix organisation. The gene list pertaining to genes that were extremely upregulated for B alone did not produce significant pathways or processes that could be included in the heatmap.

3.3.3.2. Time course of the fold-change for pBMSCs on the scaffolds. To evaluate the evolution of gene expression levels over time, genes displaying a statistically significant difference at 3, 7, 14, and 21 days of culture of pBMSCs on the scaffolds (T) were collected. Fig. 8 depicts the genes whose variations over time were statistically significant ($p < 0.01$) between all recorded time points. This list of genes significantly modified over time was further evaluated through pathway and process enrichment analysis following the same procedure applied in 3.3.3.1, with p-values calculated based on the cumulative hypergeometric distribution and q-values computed using the Benjamini-Hochberg procedure to account for multiple testing. After clustering the ontology terms, the most relevant ones, as representatives of the processes inside each cluster, are included in Table 1.

3.3.3.3. Modifications over time from the initial expression patterns. The expression levels on days 7, 14, and 21 were taken into account by considering the third day of culture as a reference, creating a new subset of genes with statistically significant differences ($p < 0.05$) between time points. The analysis identified four patterns of expression: sets of genes displaying an increased trend of upregulation compared to the initial state (CPS1, EYA2, ADAM19, ATP8B1, PTPRN, LAMA2, NDUFA4L2, BX322234.1, PAX8-AS1, SORCS2, SLIT2, RNF150), a decreasing positive expression (CALB2, OLFML3), a sustained upregulation throughout all time points (MT-TT, CHRNA1, SERPINB7, SLC7A4, DKK2, ACTG2), or an initial downregulation followed by positive modifications (MEOX2, RGS16) (Figs. S9–S12).

The results of the present part of the study demonstrated that the β-TCP scaffold supported pBMSCs' viability and promoted extracellular matrix organisation, with transcriptomic analysis highlighting gene expression patterns associated with cell adhesion, migration, and extracellular matrix remodeling. However, the scaffold did not induce strong osteogenic differentiation.

3.4. *Scaffold application in 3D in vitro model of osteosarcoma*

The developed *in vitro* model design implies the use of several 'building blocks' that represent key features of the osteosarcoma

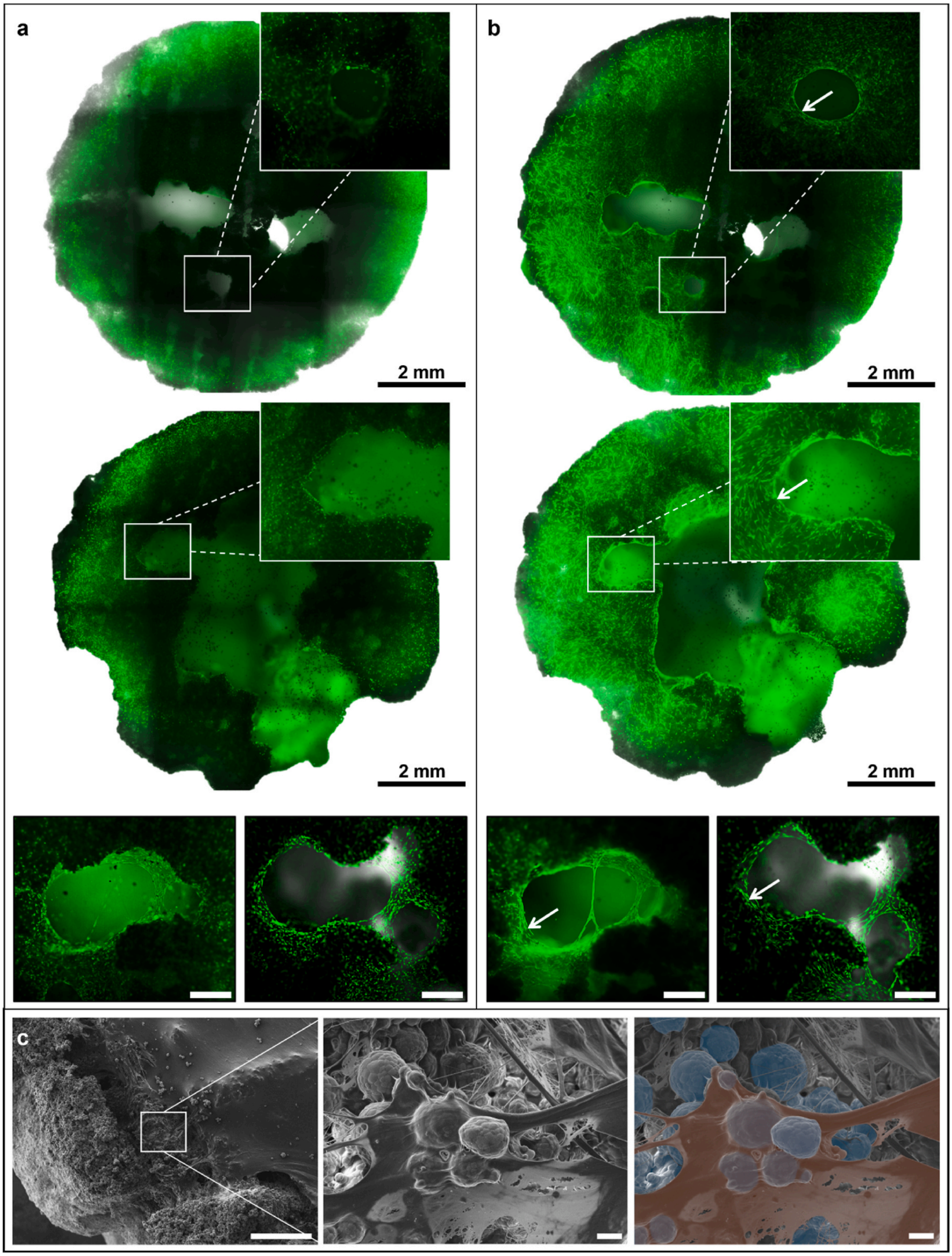

Fig. 5. – a, b: Live/dead staining of pBMSCs cultured on 3D-printed β-TCP scaffolds for 3 days (a) and for 7 days (b). White arrows indicate regions with more elongated, oriented pBMSCs and/or evidence of abundant ECM synthesis. Only the green ("live", Calcein AM) channel is presented due to the absence of the signal in the red ("dead", Ethidium homodimer-1) channel. Scale bars 2 mm (full-view images) and 500 μm (magnified images). c: SEM images of 21-d pBMSCs-seeded scaffolds. The formation of cell sheets covering the scaffold and the filling of the interspace between β-TCP granules (arrows mark the cells, asterisks mark β-TCP granules) are demonstrated at magnifications of × 50 (scale bar 500 μm) and × 1000 (framed images, scale bar 10 μm). (For interpretation of the references to colour in this figure legend, the reader is referred to the Web version of this article.)

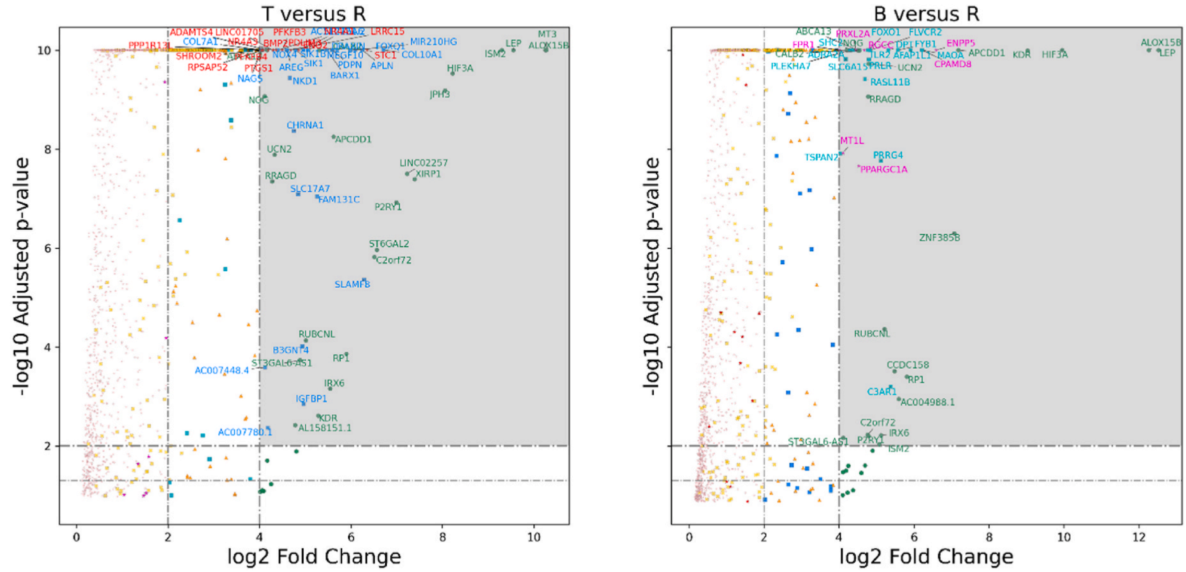

Fig. 6. – Volcano plots of upregulated genes in cells cultured on both scaffolds (T) and osteogenic medium (B) versus regular medium (R). Gene names followed the colour scheme shown in Table S2. (For interpretation of the references to colour in this figure legend, the reader is referred to the Web version of this article.)

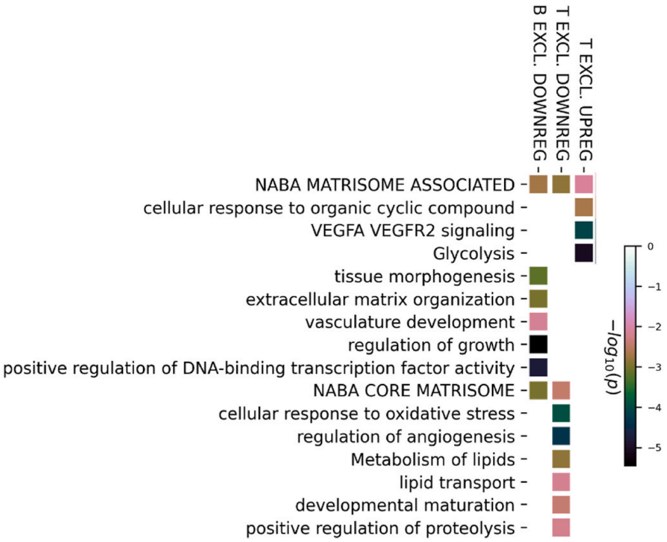

Fig. 7. – Enrichment heatmap of the most relevant clusters summarising the gene ontology terms during pathway and process enrichment analysis. Clusters were reported through the most significant term for identifying the labels. 'T' – cells cultured on the β-TCP scaffolds, 'B' – cells cultured in the osteogenic medium.

microenvironment. The 'tri-culture' described in this section contains the tumour unit represented by co-culture spheroids of osteosarcoma cells and hBMSCs; a bone-like environment represented by the 3D-printed β-TCP scaffold seeded with pBMSCs; and endothelial cells serving as a source of vascularisation. Additionally, to provide the resulting system with efficient mass transport and mechanical stimuli driven by fluid flow, scaffolds with three cellular components were placed in the chambers of the perfusion bioreactor. Here, we characterise the assembled tri-culture through evaluating cell activity, ion release and gene expression, as well as studying in detail the potential of the scaffolds to be vascularised. Finally, we apply the developed model for a cytotoxicity assay.

3.4.1. *Tri-culture on the 3D-printed β-TCP scaffolds*

The metabolic activity of the cells in both tri-culture scaffolds and monoculture (only U2OS-MSC spheroids, without pBMSCs and endothelial cells) demonstrated an overall positive trend, with the bioreactor slightly enhancing cell metabolic activity in the tri-culture scaffolds (Fig. 9, b). Regarding fluorescence microscopy observations, it was possible to distinguish between osteosarcoma spheroids (Fig. 9, a, red) and cells seeded in suspension – pBMSCs and endothelial cells (Fig. 9, a, green). The spheroids were compact, and almost no floating cells were observed, indicating the integrity of the spheroids. Green-stained cells were homogeneously spread throughout the scaffolds and attached to their surfaces. Fluorescence imaging after the division of the cell-seeded scaffolds into static (cultivated under standard conditions) and dynamic (cultivated in a perfusion bioreactor) groups did not reveal any visible differences between these conditions (Fig. 9, c). In both conditions, the spheroids were found to be securely arranged within the scaffolds, and the cells seeded in suspension (pBMSCs and endothelial cells) were evenly distributed and presented in comparably similar numbers in static and bioreactor cultures. With the help of acetylated LDL-based staining, it was also possible to define endothelial cells (Fig. 9, c, magnified image) that were found to be distributed as single cells throughout the scaffold without network formation.

ICP-OES was performed on the collected culture medium to quantify the concentration of the elements of interest (calcium, phosphorus, magnesium and potassium) (Fig. 10). Regarding the tri-cultures, no significant differences were observed in ion release trends between the static and dynamic settings. Potassium was averagely constant (~250 ppm) throughout the experiment, with a mild decrease at day 13 down to ~185 ppm. Calcium and phosphorus were released, showing an increasing and approximately linear trend. Calcium ranged from ~70 to ~110 ppm for both the tri-cultures, and phosphorus from ~44 to ~127 ppm and from ~73 to ~107 ppm, respectively, for the static and dynamic settings. Magnesium content (~19 ppm) was stable up to day 7, when the beginning of a linear increase was observed until day 14, leading to a concentration of ~79 ppm. As for the spheroids, the overall amount of released ions was lower than those characterising the static and dynamic tri-cultures, with potassium being mildly released (from ~240 to ~320 ppm), and the other ions maintained an approximately constant and low concentration in the medium, always below 100 ppm.

In the analysis of the total gene expression in the tri-culture on β-TCP compared to the spheroids on β-TCP, it was observed that VEGF was slightly upregulated (Fig. 11, 'Tri-culture *vs* Spheroids'). It was also noted that VEGF expression was higher in the tri-culture models

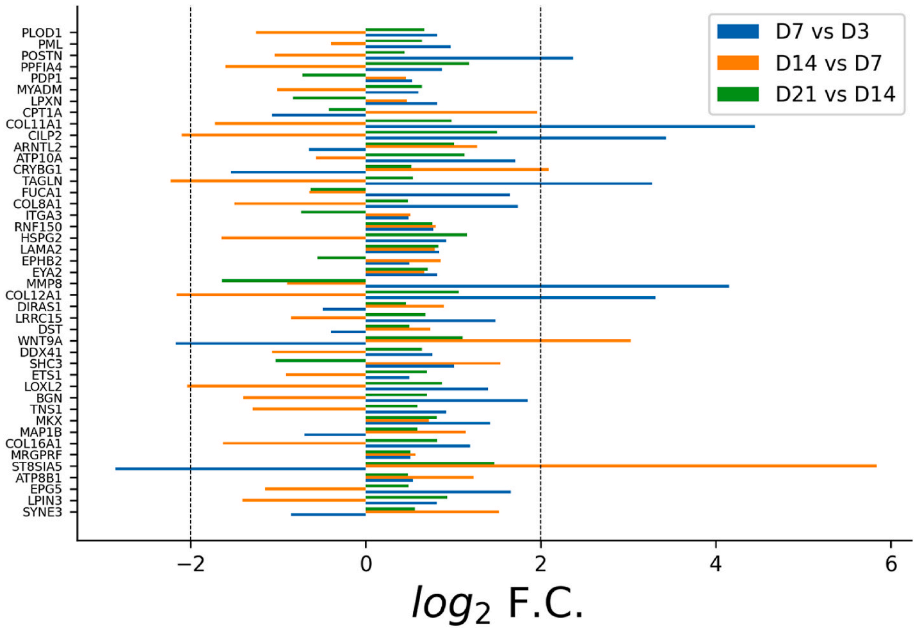

Fig. 8. – Genes significantly modified during the time course of the experiments ($p < 0.01$).

Table 1
– Enriched terms of genes showing significant differences over time.

GO	Category	Description
R-HSA-1474244	Reactome Gene Sets	extracellular matrix organization
hsa04820	KEGG Pathway	cytoskeleton in muscle cells
GO:0001666	GO Biological Processes	response to hypoxia
R-HSA-216083	Reactome Gene Sets	integrin cell surface interactions
GO:0007162	GO Biological Processes	negative regulation of cell adhesion
GO:0031099	GO Biological Processes	regeneration
GO:0034330	GO Biological Processes	cell junction organization
GO:0030335	GO Biological Processes	positive regulation of cell migration
WP185	WikiPathways	integrin-mediated cell adhesion
GO:0090596	GO Biological Processes	sensory organ morphogenesis
WP5434	WikiPathways	cancer pathways
GO:0015748	GO Biological Processes	organophosphate ester transport
WP3594	WikiPathways	circadian rhythm genes
GO:0044242	GO Biological Processes	cellular lipid catabolic process
GO:0031349	GO Biological Processes	positive regulation of defence response

incubated in a perfusion bioreactor (dynamic) than in those incubated in standard (static) conditions (Fig. 11, 'Dynamic *vs* Static'). The difference in gene expression between spheroids and tri-culture was highlighted, especially in the case of the KDR gene (2^{-ddCT} around 5000), because KDR is specific for endothelial cells, which were not present in the spheroid models (Fig. 11, 'Tri-culture *vs* Spheroids'). In addition, KDR was upregulated in static tri-culture compared to dynamic tri-culture. TP53 was upregulated in tri-culture, with a prevalence of expression under dynamic conditions. Finally, RB1 was also upregulated, with prevalence in the static tri-culture.

3.4.2. Scaffold vascularisation assay

The ability of the β-TCP scaffold to support vascularisation was assessed through an endothelial cell migration assay. This approach aimed to differentiate the effects of β-TCP scaffold chemistry from potential limitations related to scaffold volume and nutrient transport, providing insights into endothelial cell behaviour within the model.

3.4.2.1. β-TCP scaffold milling and spheroid formation. SEM analysis of the milled scaffolds revealed that milling did not cause breakage of the β-TCP granules and that their structure was maintained (Fig. S13, a). OS cell spheroids were formed in AggreWell™ 400 plates within 24 h of culturing. However, to ensure their stability, spheroids were harvested and used only after 48 h of culture. Throughout the patterning optimisation, the largest spheroids (⌀ 200 μm, formed out of 500 MGreen63 cells each) were chosen for the following applications. Their formation (in triplicates) is shown in Fig. S13, b. An example of the final cell migration assay set-up with the patterned particles of the milled β-TCP scaffold is shown in Fig. 12, a.

3.4.2.2. Image analysis. Fluorescence microscopy demonstrated the maintenance of the ring-shaped arrangement of the osteosarcoma spheroids in the chamber along with their gradual aggregation, which was more pronounced in the absence of β-TCP particles (Fig. 12, b, 'OS' and 'OS + β-TCP'). It was also observed that the patterned particles maintained the ring-shaped spatial arrangement, indifferent to the presence of the OS spheroids (Fig. 12, b, 'OS + β-TCP' and 'β-TCP'). As for endothelial cells, the most visible network formation was observed for the sample containing only spheroids (Fig. 12, b, 'OS' at 5 days). The least pronounced network development and proliferation of endothelial cells were observed in the sample containing only β-TCP particles (Fig. 12, 'β-TCP' at 5 days). Colocalization analysis performed via radial profile assay revealed no significant evolution of the HUVECs network in proximity to the patterned components (Fig. 12, c). Immunofluorescent staining with the tight junction protein PECAM-1 (CD31) with subsequent quantification of its fluorescence intensity (FI) relative to the overall fluorescence of HUVECs (RFP) demonstrated lower FI for the group containing osteosarcoma spheroids and scaffold particles in comparison to the group containing only osteosarcoma spheroids (Fig. 12, d).

In this section, a tri-culture consisting of osteosarcoma spheroids, pBMSCs and endothelial cells was assembled on the scaffolds and characterised in comparison to monoculture (only spheroids) on the scaffolds by means of cell metabolic activity, cell viability, gene

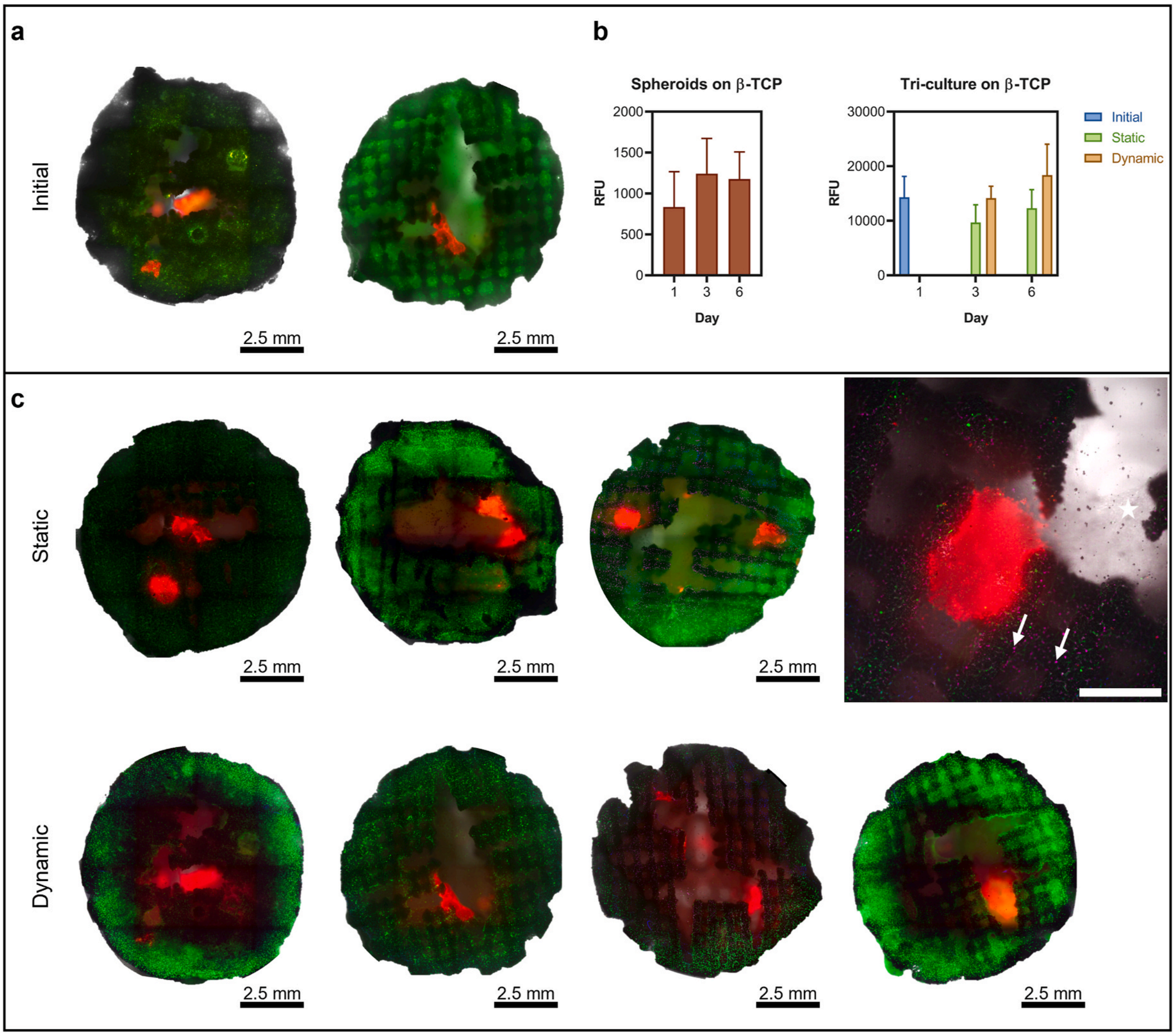

Fig. 9. – Fluorescent microscopy (a, c) and metabolic activity (b) of co-cultured U2OS-MSC spheroids and tri-culture (spheroids + pBMSCs + endothelial cells) on β-TCP scaffolds. Panels a and c: co-cultured U2OS-MSC spheroids are stained with a cell tracker and are visible in red; pBMSCs and endothelial cells are stained with Calcein AM and are visible in green; scale bars 2.5 mm. On the magnified image, endothelial cells were additionally stained with acetylated LDL and are visible in magenta (marked with arrows). The cell-produced collagen is slightly visible as semi-transparent fibres stretched between the scaffold structures (marked with a star). Scale bar 650 μm. Panel b: Values are presented as the average RFU ± SD. (For interpretation of the references to colour in this figure legend, the reader is referred to the Web version of this article.)

expression analysis and ion release, with overall evidence of a positive contribution of tri-culture and dynamic culture conditions on the physiological relevance of osteosarcoma model. Endothelial cells did not form capillary-like networks, despite elevated expression of characteristic genes. Shown further in the migration assay, endothelial cell network formation was impaired in the presence of β-TCP particles, suggesting a potential inhibitory effect of the scaffold's chemical composition.

3.4.3. Application of the tri-culture model in a cytotoxicity test

Doxorubicin (DOX) was chosen for a preliminary assessment of the tri-culture model suitability for anticancer drug cytotoxicity applications. DOX, also known as adriamycin, is frequently used for the post-surgical or presurgical treatment of osteosarcoma patients in the context of a chemotherapy course known as MAPi, a combination of methotrexate, adriamycin, cisplatin, and ifosfamide [2].

Owing to the autofluorescence of DOX, it was possible to track its accumulation in the compared groups of samples: osteosarcoma spheroids on the scaffolds and tri-culture on the scaffolds. As shown in Fig. 13, a, there was a difference in the DOX accumulation: while in the 'Spheroids' group, osteosarcoma spheroids were highly fluorescent with DOX, it did not seem to accumulate the drug while in the tri-culture. A semi-quantitative analysis of the DOX accumulation was performed on the images. Surface plots based on the fluorescence intensity demonstrated the localisation of the fluorescent signal – concentrated in the specific area in the case of the 'Spheroids' group and scattered in the case of the 'Tri-culture' group (Fig. 13, b). The images were further converted to binary, and particles were counted in triplicate, corresponding to highly fluorescent cells – 149 ± 58 counts for monoculture and 29 ± 12 counts for tri-culture (here reported with SD).

Additionally, similar to 3.4.1, the release of calcium, phosphorus, magnesium and potassium ions was characterised for the samples exposed to DOX, and no significant difference was observed compared to the control samples not exposed to DOX (Fig. S14).

4. Discussion

Despite advances in cancer research, osteosarcoma therapy has seen little progress in recent decades. This stagnation highlights the need for innovative preclinical models that, on one hand, align with the 3R principle and solve the lack of translatability of *in vivo* models, and, on the other hand, better replicate the tumor microenvironment compared

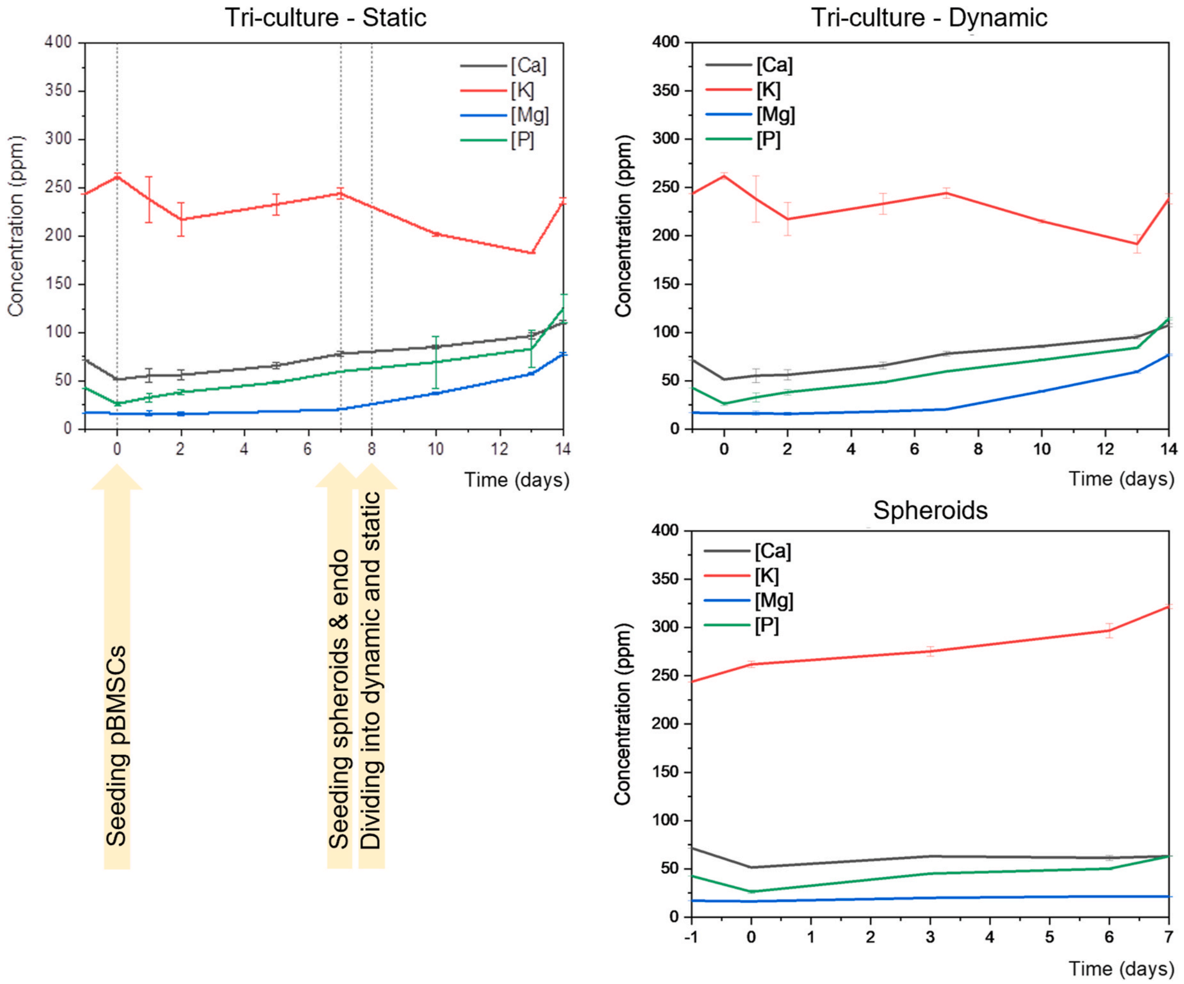

Fig. 10. – ICP-OES of medium collected from U2OS-MSC spheroids (‘Spheroids’) and tri-culture (spheroids + pBMSCs + endothelial cells, ‘Tri-culture’) cultured on β-TCP scaffolds in standard conditions (‘Static’) or bioreactor (‘Dynamic’). Day ‘-1’ corresponds to the culture medium as it is; day ‘0’ – to the medium in which the scaffold was pre-incubated without cells for 24 h; day ‘N’ (with N ranging from 1 to 14 days of culture) – to the medium where cells were cultivated for N day on the scaffold. The values are presented as the average of three replicates, and the bars represent the SD.

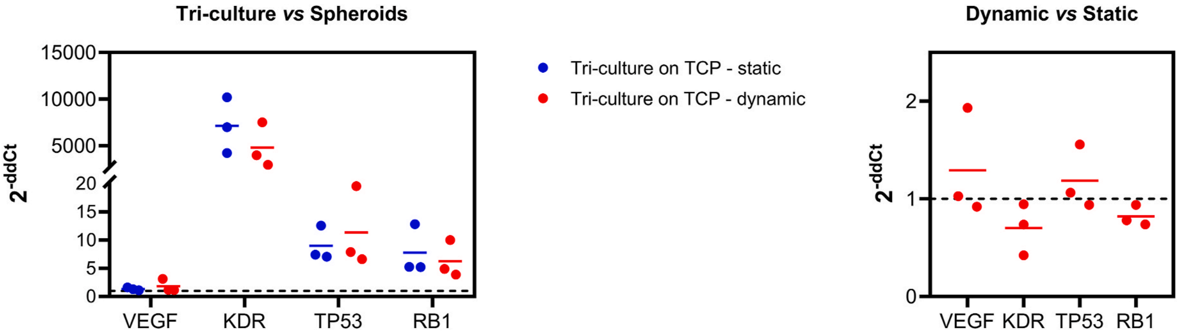

Fig. 11. – Normalised gene expression in tri-cultures on β-TCP scaffolds in relation to osteosarcoma spheroids on β-TCP scaffolds (left) and dynamic tri-cultures in relation to static tri-cultures (right). ACTB was used as the housekeeping gene. The data are presented as the 2^{-ddCt} for each sample and their means.

to conventional 2D models. 3D *in vitro* models present a promising avenue for improving drug testing and understanding osteosarcoma biology. Existing approaches include scaffold-free spheroid cultures [25–27] (including co-culture spheroids made from different cell types [28–30]); scaffold-based approaches [31–34], organoid-based, microfluidic and bioreactor systems [35–37], to name a few, each with strengths and limitations in mimicking key components of the osteosarcoma microenvironment *in vivo*. In our study, we attempted to build a step-by-step *in vitro* model by combining a bone-like environment (3D-printed β-TCP scaffold seeded with primary bone marrow-derived MSCs), a tumour-like unit (osteosarcoma cell spheroid), a source of vascularisation (endothelial cells), and physiological stimuli (perfusion bioreactor).

The main focus of the present study was to investigate the potential of the 3D-printed β-TCP scaffold to mimic bone tissue in the context of the developed preclinical platform. Trabecular bone exhibits 30 %–95 % porosity, with pore sizes ranging from 200 to 1000 μm [38]. This porosity facilitates nutrient transport, waste removal, and

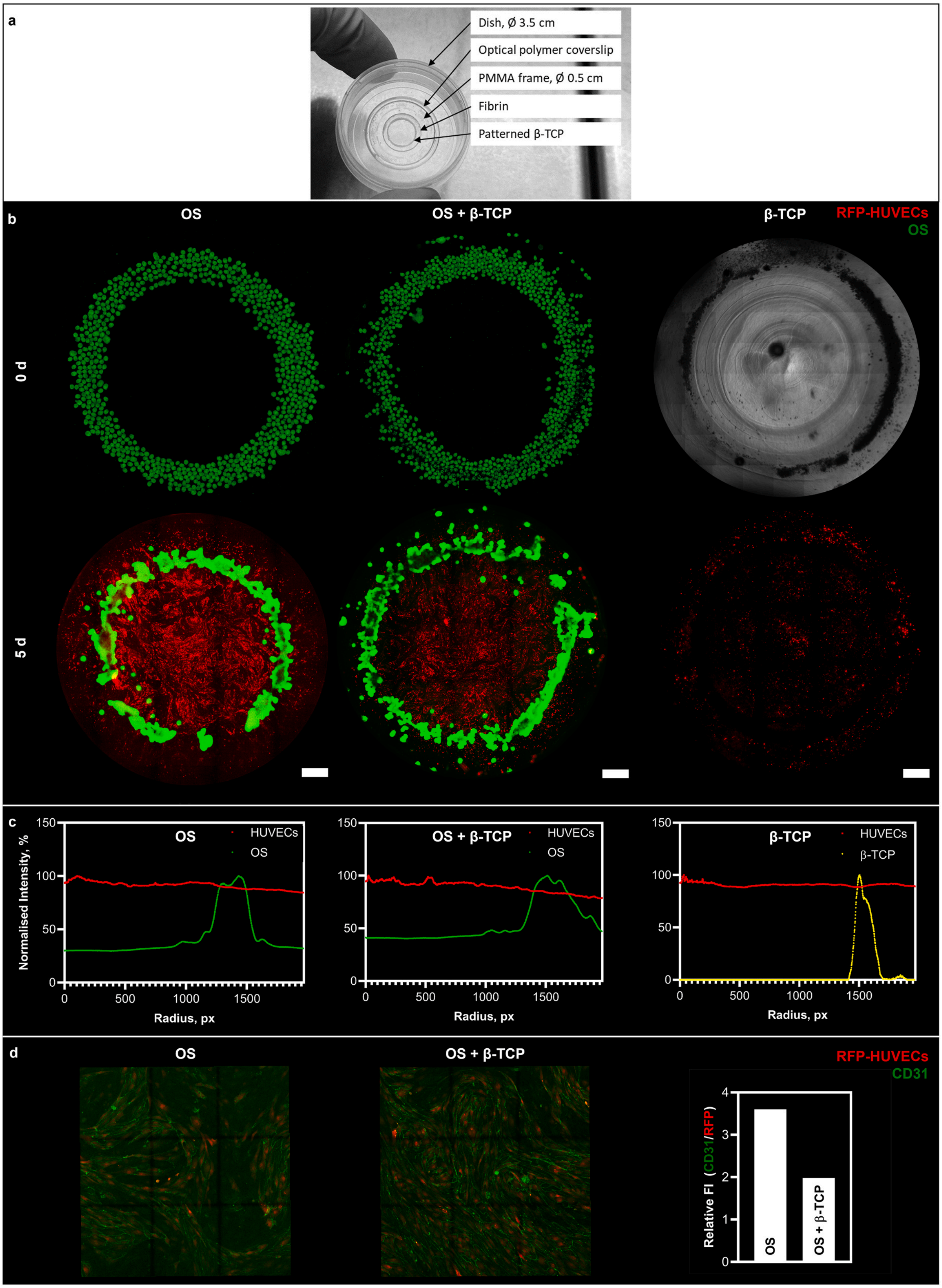

Fig. 12. – a: Resulting pattern of β-TCP particles in fibrin. b: Overview of the three conditions (patterned spheroids, ‘OS’, patterned particles, ‘β-TCP’, and spheroids and particles patterned together, ‘OS + β-TCP’) on days 0 and 5. Transmitted light (‘β-TCP’ at day 0) and fluorescence microscopy; scale bar: 1 mm. c: Radial profile analysis of three conditions at the final point of the experiment (5 days). d: Immunofluorescence microscopy with CD31 (PECAM-1) relative fluorescence intensity reported for groups ‘OS’ OS ‘OS + β-TCP’; HUVECs are visible in red, and expressed CD31 is visible in green. (For interpretation of the references to colour in this figure legend, the reader is referred to the Web version of this article.)

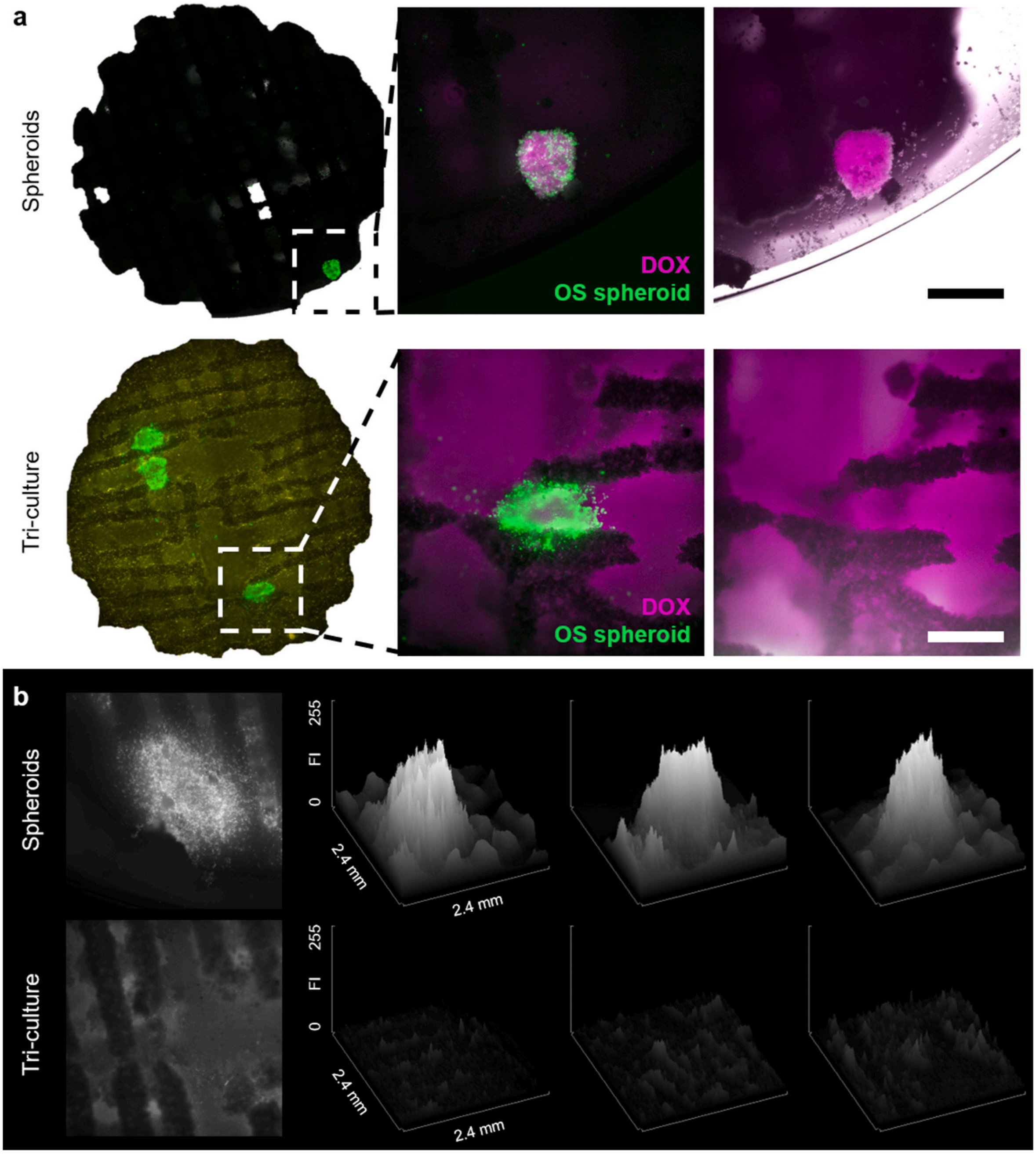

Fig. 13. – a: Fluorescent microscopy of co-culture U2OS-MSC spheroids (‘Spheroids’) and tri-culture (‘Tri-culture’) on β-TCP scaffolds exposed to DOX. Co-cultured U2OS-MSC spheroids are visible in green; pBMSCs and endothelial cells are visible in olive green. DOX accumulation is visible in magenta in the magnified image. Scale bar 650 μm. b: surface plots demonstrating localisation of DOX fluorescence in ‘Spheroids’ and ‘Tri-culture’ samples. Fluorescence intensity is represented by grey values (z-axis), while the x-y plane reflects the area of the analysed image. (For interpretation of the references to colour in this figure legend, the reader is referred to the Web version of this article.)

vascularisation, with pores larger than 100 μm promoting bone ingrowth and 200–600 μm being ideal for angiogenesis and osteogenesis [39]. In turn, roughness and nano-/microscale features of biomaterials are known to influence protein adsorption, integrin-mediated signalling, cell adhesion, ECM protein deposition, and subsequent osteogenic differentiation [40]. Hence, from a structural point of view, by demonstrating the presence of interconnected macropores in the scaffold, and a porosity in line with the physiological porosity of human bone [38], as well as microstructures forming convex and concave roughness features of the surface, and even the distribution of the key chemical elements over them, we forecasted – and confirmed in the following *in vitro* assays – that such features would be beneficial for subsequent cell culture studies by facilitating cell attachment, spreading, and integration into the scaffold structure. Furthermore, the results of FTIR-ATR and XRD analyses allowed us to conclude that the chemical composition and crystalline structure of β-TCP were preserved throughout scaffold manufacturing. Indeed, FTIR-ATR spectroscopy (Fig. 2) clearly shows the typical vibrations of β-TCP, post-sintering. All bands assigned to the pl30 matrix, seen before sintering, fully disappear after sintering, confirming the full decomposition and evaporation of the matrix. It should also be mentioned that, visually, the scaffolds post-sintering appear white in color, indicating that no carbon remains after burning of the pl30 matrix.

It is worth noting that along with the microstructural and chemical properties of the scaffold, its stiffness plays an important role in the cell fate [41]. The molecular signalling of cells, as well as their migration and differentiation, may be altered by the stiffness of the surrounding matrix owing to mechanotransduction mechanisms that transform mechanical stimuli into biochemical cues [42,43]. In the context of osteosarcoma, the cellular-scale stiffness of the surrounding ECM plays a key role for both normal bone tissue-residing cells and cancer cells. Matrix stiffness directly affects attachment and differentiation of MSCs [44,45], as well as growth and invasiveness of cancer cells [46–48]. It was demonstrated in a series of *in vitro* models of osteosarcoma that the relatively high stiffness of the used substrate impacts cancer cells' activity, biomarker expression, and invasiveness [32–34,49–51]. Thus, in osteosarcoma modelling, a scaffold serving as a microenvironment for the bioengineered tumour unit is expected to exhibit stiffness higher than that of the tumour unit itself. Although it was difficult to accurately define the β-TCP scaffold stiffness by the nanoindentation method due to the scaffold's highly porous structure, it was demonstrated that the values lie in the range of MPa (66.46 ± 29.26 MPa, Fig. 3, e). The compression test showed Young's modulus values in the same order as those measured via nanoindentation (11.17 ± 2.90 MPa). The demonstrated values are lower than the typical parameters of bone tissue *in vivo* [52–55] and of the values reported earlier for TCP-based materials [56,57]; however, they are sufficient to make the scaffold stiffer than the cell spheroids [36,37] by an order of magnitude on both micro- and macroscales, which fulfils the purpose of the current study.

We further evaluated the suitability of the scaffold for *in vitro* applications using a cytocompatibility assay via direct contact with cells. Considering the future perspectives of scaffold usage, that is, employing them as a bone-like matrix for the osteosarcoma model, two cell lines were chosen for the preliminary studies: human osteosarcoma (U2OS) and human bone marrow-derived mesenchymal stem cells (hBMSCs). The decrease in the metabolic activity of hBMSCs on the scaffolds was related to inefficient mass transport in the conditions of standard (static) culture with a limited culture medium volume (Fig. 4, a). Considering that the number of hBMSCs seeded in suspension drastically exceeded the number of U2OS cells used for spheroid generation, it was expected that the cells would become less metabolically active over time. Moreover, the decrease in hBMSCs' metabolic activity could be a result of their minor osteogenic stimulation by the β-TCP scaffold, as will be discussed below. In contrast, in the case of spheroids, the surrounding scaffold could serve as a support for further growth and proliferation, and, again, due to the comparably lower number of cells, the volume of the culture medium seemed to be sufficient to explain the gradual increase in spheroid metabolic activity. Fluorescence microscopy imaging (Fig. 4, b) revealed hBMSCs attachment, elongated morphology, and homogeneous spread within the scaffold, which was important in the context of the engineered bone tissue and correlated with our earlier predictions based on information about the scaffold's structural analysis. Next, when discussing the tumour unit (which is represented by the cell spheroid in the developed model), we are seeking the maintenance of the cell spheroid within the scaffold along with its integration into the surrounding environment. It was observed that after 7 days of culture, osteosarcoma spheroids remained aggregated, but at the same time attached to the scaffold surface (Fig. 4, c).

To obtain a deeper understanding of the MSCs' behaviour inside the bone-mimicking scaffolds, we seeded primary MSCs for a prolonged period of culture. At this stage, we observed a positive trend in the metabolic activity of cells (in contrast to the previously demonstrated decrease in the activity of immortalised MSCs) on the scaffolds (Fig. S3). We also confirmed the need for an optimisation step, that is, preparatory immersion of the scaffolds in a serum-rich medium. This step might have prevented excessive adsorption of the proteins from the culture medium, which could lead to a lack of nutrients and cell starvation. Based on visual observations via fluorescence and scanning electron microscopy (Fig. 5), we determined the intensive synthesis of ECM by pBMSCs, indicating pronounced cell metabolic activity. Calcium phosphates are known for their potential to trigger MSC differentiation along the osteoblastic lineage [6]. Therefore, we evaluated the activity of alkaline phosphatase (ALP), an early marker of osteogenic differentiation, in pBMSCs on the β-TCP scaffold. Indeed, with the overall increase in ALP activity, among the points analysed, we observed the peak at the earliest point, which might indicate the start of osteogenic differentiation (Fig. S4).

We further analysed the processes activated in pBMSCs during their culture on the β-TCP scaffolds. By comparing the RNA-Seq data of pBMSCs on the scaffolds with pBMSCs cultured in an osteogenic medium in relation to cells in a regular medium, we sought similarities in terms of osteogenic differentiation (Figs. 6 and 7). Interestingly, the scaffolds did not seem to directly promote cell differentiation along the osteoblastic lineage, and functional analysis of genes commonly upregulated or downregulated in the compared groups revealed only pathways involved in calcium ion homeostasis. The other highly activated pathways were not relevant to the desired differentiation processes (for instance, cues involving VEGF and VEGFR signalling) but were still important for understanding cell behaviour in the assembly of the triculture model (for example, the pathways related to angiogenesis were downregulated in the pBMSCs on the β-TCP scaffolds in comparison to cells in regular media). Nevertheless, the analysis of gene expression as a function of time, which was performed by analysing RNA extracted from several points in the experiment, demonstrated a strong involvement of cell migration and adhesion regulation, integrin cell surface interaction, and ECM organisation processes that correlated with the visual observations of the pBMSC-seeded scaffolds (Fig. 8). In addition, we observed that genes activated throughout the experiment were upregulated, downregulated, or sustained during the 3-week cultivation of pBMSCs on the scaffolds (Figs. S9–S12). Among the genes with increasing expression patterns over time, the genes of interest included ADAM19, LAMA2, NDUFA4L2, and SLIT2. ADAM19-encoded proteins are involved in various cellular processes, such as cell migration and cell-cell and cell-matrix adhesion, may be associated with chondrogenesis and were found to be present in osteoblasts [58,59]. LAMA2-encoded proteins are involved in cell attachment, migration, and organisation in tissue formation processes, as well as play a role in the interaction with ECM, and have been shown to inhibit osteogenesis and promote adipogenesis [60]. Thus, the upregulation of LAMA2 and, less likely, ADAM19 may serve as additional evidence for the lack of osteogenic differentiation of pBMSCs on the scaffolds. In contrast, SLIT2 up-regulation may promote osteogenic differentiation [61]. In turn, NDUFA4L2 may be of interest in the context of co-culture because it has been shown to facilitate the EMT of osteosarcoma cells [62]. Additionally, there were genes with increasing expression patterns that were markedly downregulated at the beginning of the experiment (day 7). Among them, we focused on MEOX2 and RGS16. MEOX2 is thought to be involved in the inhibition of bone formation [63], whereas RGS16 is expressed in osteoblasts and osteoprogenitor cells [64]. Among the genes with decreasing behaviour, our interest was drawn to CALB2 and OLFML3. CALB2 encodes calbindin 2, an intracellular calcium-binding protein that buffers the rise of Ca^{2+} intercellular levels [65] but also plays a role in neuroprotection in MSCs [66], while the OLFML3-encoded scaffold protein may be involved in recruiting bone morphogenic protein-1 and may promote endothelial cell proliferation and migration [67]. Downregulation of the latter may be an obstacle in the engineering of vascularised tissues. Among the genes that showed sustained over-expression at all time points, we focused on DKK2, which is involved in the terminal stages of osteoblast differentiation [68]. Overall, these results indicate a very mild direct activation of osteogenic differentiation along with pronounced ECM synthesis and tissue formation, as well as providing hints for consideration in co-culture assembly.

An intermediate conclusion regarding the positive outcome of the developed *in vitro* model assembly was based on the results of cell metabolic activity and cell viability (Fig. 9). Both spheroid 'monoculture' on the scaffolds and tri-culture (spheroids on the scaffolds seeded with pBMSCs and endothelial cells) demonstrated a positive trend in metabolic activity with a slight indication of the beneficial impact of dynamic conditions achieved by perfusion bioreactor (Quasi Vivo® system). However, along with the satisfactory morphology of both co-cultured osteosarcoma spheroids and pBMSCs, endothelial cells did not proliferate or form a capillary-like network. Endothelial cell network formation in 3D *in vitro* models is frequently stimulated by the addition of either matrix components, such as fibronectin, or growth factors, such as vascular endothelial growth factor (VEGF), and these measures might facilitate the formation of the network in the present model [69,70]. Although VEGF expression was demonstrated in the RT-qPCR analysis (Fig. 11) and was elevated in the tri-culture on the scaffold in comparison to the spheroids on the scaffold, this might not be sufficient to trigger the growth of the vessel-like structure. KDR encodes a receptor for VEGF. KDR expression is elevated in endothelial cells recruited to sites of VEGF-mediated angiogenesis. Both circulating VEGF and KDR are markers of the efficacy of anticancer drugs targeting angiogenesis [71]. The overexpression of KDR in the tri-culture pointed to the survival and functional state of endothelial cells, even though we did not observe their characteristic morphology via microscopic analysis. Interestingly, KDR was upregulated in static tri-culture compared to dynamic tri-culture, which might indicate better survival of endothelial cells under static conditions, inhibition of their activity in perfusion conditions, or both. The tumour suppressor protein p53, a cellular tumour antigen, is encoded by TP53. In response to various cellular stressors, p53 modulates target gene expression, consequently triggering various biological processes, such as cell cycle arrest, apoptosis, senescence, DNA repair, and metabolic alterations. Upregulation of TP53 is associated in the context of osteosarcoma with a decreased 3-year disease-free survival as well as a shorter 3-year overall survival [72]. TP53 was found to be upregulated in tri-culture, with a prevalence of expression in dynamic conditions. Retinoblastoma-associated protein (RB1 gene) is a tumour suppressor and a major modulator of the G1/S phase of the cell cycle. Owing to its role, RB1 is anticipated to be either downregulated or mutated in a broad range of malignancies, including osteosarcoma. Additionally, RB1 is a possible indicator of osteosarcoma metastasis [73]. RB1 was also upregulated, with a prevalence in static tri-culture. Considering the above-listed evidence of the correlation of marker expression with the invasiveness of the tumour, it appears that tri-culture is beneficial for approximating the tumour-like behaviour of osteosarcoma spheroids, at least, judging from VEGF, KDR, and TP53 expression. It is not clear whether the upregulation of RB1 should be considered as a "negative" characteristic of the developed model, and further investigation should be performed.

In the ICP-OES analysis of tri-culture scaffolds, no significant differences were noted in ion release between static and dynamic conditions (Fig. 10). However, distinct differences were observed when comparing these tri-culture scaffolds to monoculture scaffolds containing only spheroids. In monoculture, calcium and phosphorus levels remained constant, whereas in tri-culture, their concentrations showed a mild increase over time under both static and dynamic conditions. This trend is consistent with scaffold degradation occurring progressively in an aqueous environment, which releases calcium and phosphorus, the primary components of the TCP network [74]. The inclusion of additional cell types in the tri-culture may have elevated the local pH due to active cell metabolism, potentially accelerating β-TCP scaffold degradation and dissolution compared to that seen in spheroid-only cultures. Potassium levels in the tri-culture did not significantly change over time, likely because the culture medium was the sole source of this ion. Regular metabolic activity of the cells appeared to maintain these levels, with minor fluctuations possibly indicating cellular adaptation to the scaffold. This behaviour supports the biomimicry of the engineered model, where cellular responses mirror those seen *in vivo*. In contrast, potassium levels in the spheroid monoculture increased by the end of the experiment. Since potassium efflux is linked to apoptosis, this may suggest that spheroids experienced cellular stress under monoculture conditions [75]. Another possible explanation relates to the Warburg effect, a feature of cancer cell metabolism. The high metabolic activity characteristic of this effect can significantly alter intracellular ion balance, prompting potassium efflux to restore stability. Additionally, the buildup of glycolytic intermediates and lactate can disrupt osmotic equilibrium, leading to potassium efflux as a cell volume regulatory response [76]. Magnesium concentration stayed consistently low in spheroid-only cultures. Notably, in the tri-culture, magnesium levels, which remained stable until day 7, began to increase linearly after the spheroids and endothelial cells were added. Magnesium homeostasis is critical for various metabolic processes and ion exchange, yet the mechanisms underlying its efflux under different culture conditions remain poorly understood [77,78]. The observed magnesium release in the tri-culture compared to its stability in monoculture most likely reflects a more active degradation of medium components due to overall higher cell metabolic activity and more complex cellular interactions. However, a comprehensive analysis of ion exchange dynamics and cellular signalling pathways is required to fully explain these differences.

Next, we aimed to determine the possible inhibition of endothelial network formation by the chemical composition of the scaffold, uncoupling it with the factor of the scaffold volume that could potentially limit the transport of nutrients and oxygen, thereby impairing the functionality of endothelial cells [79,80]. For this, we performed an endothelial cell migration assay by tracking the location of the cells relative to ring-patterned osteosarcoma spheroids, β-TCP particles, or both. We discovered that there might be an inhibiting effect from the side of the β-TCP, judging from the overall poorer cell network formation and lower expression of tight junction protein PECAM-1 (CD31) in the endothelial cells compared to the sample containing osteosarcoma spheroids only (Fig. 12). Moreover, based on the results of RNA-Seq analysis performed on pBMSCs cultured on the scaffold, the overall inhibition of vascularisation may occur indirectly via signalling between endothelial cells and pBMSCs. We observed that angiogenesis-related pathways were downregulated in pBMSCs cultured on the scaffolds compared to pBMSCs cultured under regular conditions. Moreover, in a 3-week course of gene expression evolution, we defined downregulated OLFML3 as encoding a protein which is thought to enhance the activity of endothelial cells and angiogenesis [81].

Finally, we applied the developed *in vitro* model as an advanced preclinical investigation platform to assess the toxicity of the widely used anticancer drug doxorubicin (DOX). By tracking the fluorescence signal of the accumulated drug, we observed high fluorescence intensity of the osteosarcoma spheroids cultured on the scaffolds in the absence of pBMSCs and endothelial cells, indicating pronounced accumulation of the drug in the spheroids (Fig. 13, a and b, upper panels). In contrast, when analysing the accumulation of DOX in the tri-culture scaffolds, only a background fluorescent signal was observed and no signal coming from the osteosarcoma spheroids, indicating that there was little or no DOX accumulated in the spheroids when cultured as a part of the tri-culture (Fig. 13, a and b, lower panels). The native tumour microenvironment is shaped by orchestrating multiple cell types. For instance, endothelial cells contribute to vascularisation and transport of nutrients and drugs, whereas MSCs often play a supportive role in influencing tumour progression and drug resistance [36]. By including these cell types in the tri-culture, we aimed to replicate aspects of the tumour microenvironment that affect drug penetration and distribution within tumours. The reduced accumulation of DOX in the tri-culture could indicate that the model better approximated the barriers present *in vivo*, such as the extracellular matrix or cellular uptake competition [82]. Osteosarcoma spheroids in monoculture are isolated and lack physiological barriers, allowing DOX to penetrate and accumulate relatively freely. In contrast, in tri-culture, endothelial cells and pBMSCs may create additional layers, higher affinity or secretions that reduce drug penetration into the spheroids [83]. Even though we did not develop a vascular-like barrier by endothelial cells, we observed that pBMSCs secreted extracellular matrix, as shown in microscopy observations (Fig. 5) and transcriptomic analysis (Fig. 7), thus influencing drug distribution. Similar contribution of MSC-synthesised ECM to the sensitivity of the osteosarcoma spheroids to DOX was demonstrated earlier by Cortini et al. in a spheroid-based co-culture model [84]. *In vivo*, chemotherapeutics, such as DOX, often exhibit uneven distribution due to limited penetration into solid tumours, vascular barriers, and drug sequestration by surrounding stromal cells [85,86]. The observation that spheroids in the tri-culture model failed to accumulate as much DOX as monoculture spheroids suggests that the tri-culture may better reflect these complex distribution dynamics, compared to the overly simplistic diffusion observed in monoculture spheroids. Therefore, these results point to the assumption that the tri-culture consisting of spheroids, pBMSCs and endothelial cells cultured on the 3D-printed β-TCP scaffolds is a more physiological-like representation of osteosarcoma compared to the 'monoculture' spheroids on the scaffolds, allowing for a more relevant and accurate preclinical screening of new therapeutic agents.

In summary, we demonstrated the feasibility of using a 3D-printed β-TCP scaffold to create a physiologically relevant *in vitro* osteosarcoma model. The scaffold effectively mimicked key aspects of the bone microenvironment, supporting pBMSCs attachment, ECM deposition, integration with osteosarcoma spheroids, and, ultimately, contributing to a realistic distribution of DOX. However, several limitations should be acknowledged. First, β-TCP exhibited an inhibitory effect on endothelial cell activity, as observed in two different endothelial cell lines used in the study (TIME-GFP and HUVEC), highlighting a potential challenge in vascularisation. Additionally, although two osteosarcoma cell lines were used (U2OS and MG63), introducing other lines to the model, such as the commercial SaOS-2 or patient-derived cells, could improve its translational relevance. This aspect represents both a shortcoming and a strength, as the developed scaffold-based system is flexible, allowing various cell types to be incorporated based on specific research needs. Lastly, a balance must be maintained between increasing model complexity to enhance physiological relevance and avoiding excessive variability, which could hinder reproducibility and data interpretation. Finding the right balance remains critical for advancing *in vitro* osteosarcoma modelling.

5. Conclusion

This study validated the use of 3D-printed β-TCP scaffolds as a bone-mimicking environment in an engineered osteosarcoma model. The physicochemical and biological properties of the scaffolds were found to be optimal for compatibility with pBMSCs, osteosarcoma spheroids, and endothelial cells, demonstrating the successful integration of these components into a tri-culture system. Transcriptomic analysis revealed key gene expression patterns linked to ECM organisation and cell adhesion, confirming the role of the scaffold in shaping the cellular microenvironment. The tri-culture model exhibited enhanced metabolic activity under perfusion conditions and altered drug accumulation, thereby emphasising its physiological relevance. Despite the need for further optimisation, particularly in promoting endothelial network formation, this study highlights the potential of β-TCP scaffolds for advanced *in vitro* tumour modelling.

CRediT authorship contribution statement

Ksenia Menshikh: Writing – review & editing, Writing – original draft, Visualization, Investigation, Formal analysis. **Virginia Alessandra Gobbo:** Writing – review & editing, Writing – original draft, Visualization, Investigation, Formal analysis. **Mauro Nascimben:** Writing – review & editing, Writing – original draft, Visualization, Investigation, Formal analysis. **Markus Hannula:** Investigation, Formal analysis. **Andrea Cochis:** Writing – review & editing, Funding acquisition, Conceptualization. **Tiziano Serra:** Writing – review & editing, Funding acquisition, Conceptualization. **Jonathan Massera:** Writing – review & editing, Funding acquisition, Conceptualization. **Abhay Pandit:** Writing – review & editing, Funding acquisition, Conceptualization. **Lia Rimondini:** Writing – review & editing, Funding acquisition, Conceptualization.

Data statement

The data that support the findings of this study are available upon request.

Declaration of competing interest

The authors declare that they have no known competing financial interests or personal relationships that could have appeared to influence the work reported in this paper.

Acknowledgements

The authors acknowledge financial support from the European Union's Horizon 2020 research and innovation programme under the Marie Skłodowska-Curie grant agreement No. 860462 (PREMUROSA). The authors extend their gratitude to Prof. Martin Stoddart and Dr Elena Della Bella (Regenerative Orthopaedics, AO Research Institute Davos, Switzerland) for kindly providing MGreen63 cells.

Appendix A. Supplementary data

Supplementary data to this article can be found online at https://doi.org/10.1016/j.mtbio.2025.101766.

Data availability

Data will be made available on request.

References

[1] L. Ewart, A. Apostolou, S.A. Briggs, C.V. Carman, J.T. Chaff, A.R. Heng, S. Jadalannagari, J. Janardhanan, K.-J. Jang, S.R. Joshipura, M.M. Kadam, M. Kanellias, V.J. Kujala, G. Kulkarni, C.Y. Le, C. Lucchesi, D.V. Manatakis, K. K. Maniar, M.E. Quinn, J.S. Ravan, A.C. Rizos, J.F.K. Sauld, J.D. Sliz, W. Tien-Street, D.R. Trinidad, J. Velez, M. Wendell, O. Irrechukwu, P.K. Mahalingaiah, D. E. Ingber, J.W. Scannell, D. Levner, Performance assessment and economic analysis of a human Liver-Chip for predictive toxicology, Communications Medicine 2 (2022) 154, https://doi.org/10.1038/s43856-022-00209-1.

[2] V.L. Tippett, L. Tattersall, N.B. Ab Latif, K.M. Shah, M.A. Lawson, A. Gartland, The strategy and clinical relevance of in vitro models of MAP resistance in osteosarcoma: a systematic review, Oncogene 42 (2023) 259–277, https://doi.org/10.1038/s41388-022-02529-x.

[3] P.-J.H. Zushin, S. Mukherjee, J.C. Wu, FDA Modernization Act 2.0: transitioning beyond animal models with human cells, organoids, and AI/ML-based approaches, J. Clin. Investig. 133 (2023), https://doi.org/10.1172/JCI175824.

[4] K. Menshikh, I. Banicevic, B. Obradovic, L. Rimondini, Biomechanical aspects in bone tumor engineering, Tissue Eng Part B Rev (2023), https://doi.org/10.1089/ten.teb.2023.0106.

[5] T. Chow, I. Wutami, E. Lucarelli, P.F. Choong, S. Duchi, C. Di Bella, Creating *in vitro* three-dimensional tumor models: a guide for the biofabrication of a primary osteosarcoma model, Tissue Eng Part B Rev 27 (2021) 514–529, https://doi.org/10.1089/ten.teb.2020.0254.

[6] M. Bohner, B.L.G. Santoni, N. Döbelin, β-tricalcium phosphate for bone substitution: synthesis and properties, Acta Biomater. 113 (2020) 23–41, https://doi.org/10.1016/j.actbio.2020.06.022.

[7] C. Paredes, J. Roleček, P. Miranda, Improving the strength of β-TCP scaffolds produced by Digital Light Processing using two-step sintering, J. Eur. Ceram. Soc. 44 (2024) 2571–2580, https://doi.org/10.1016/j.jeurceramsoc.2023.11.028.

[8] S. James, J. Fox, F. Afsari, J. Lee, S. Clough, C. Knight, J. Ashmore, P. Ashton, O. Preham, M. Hoogduijn, R.D.A.R. Ponzoni, Y. Hancock, M. Coles, P. Genever, Multiparameter analysis of human bone marrow stromal cells identifies distinct immunomodulatory and differentiation-competent subtypes, Stem Cell Rep. 4 (2015) 1004–1015, https://doi.org/10.1016/j.stemcr.2015.05.005.

[9] M. Ashburner, C.A. Ball, J.A. Blake, D. Botstein, H. Butler, J.M. Cherry, A.P. Davis, K. Dolinski, S.S. Dwight, J.T. Eppig, M.A. Harris, D.P. Hill, L. Issel-Tarver, A. Kasarskis, S. Lewis, J.C. Matese, J.E. Richardson, M. Ringwald, G.M. Rubin, G. Sherlock, Gene Ontology: tool for the unification of biology, Nat. Genet. 25 (2000) 25–29, https://doi.org/10.1038/75556.

[10] M. Kanehisa, KEGG: kyoto encyclopedia of genes and genomes, Nucleic Acids Res. 28 (2000) 27–30, https://doi.org/10.1093/nar/28.1.27.

[11] A. Fabregat, S. Jupe, L. Matthews, K. Sidiropoulos, M. Gillespie, P. Garapati, R. Haw, B. Jassal, F. Korninger, B. May, M. Milacic, C.D. Roca, K. Rothfels, C. Sevilla, V. Shamovsky, S. Shorser, T. Varusai, G. Viteri, J. Weiser, G. Wu, L. Stein, H. Hermjakob, P. D'Eustachio, The reactome pathway knowledgebase, Nucleic Acids Res. 46 (2018) D649–D655, https://doi.org/10.1093/nar/gkx1132.

[12] A. Subramanian, P. Tamayo, V.K. Mootha, S. Mukherjee, B.L. Ebert, M.A. Gillette, A. Paulovich, S.L. Pomeroy, T.R. Golub, E.S. Lander, J.P. Mesirov, Gene set enrichment analysis: a knowledge-based approach for interpreting genome-wide expression profiles, Proc. Natl. Acad. Sci. 102 (2005) 15545–15550, https://doi.org/10.1073/pnas.0506580102.

[13] A. Ruepp, B. Waegele, M. Lechner, B. Brauner, I. Dunger-Kaltenbach, G. Fobo, G. Frishman, C. Montrone, H.-W. Mewes, CORUM: the comprehensive resource of mammalian protein complexes—2009, Nucleic Acids Res. 38 (2010) D497–D501, https://doi.org/10.1093/nar/gkp914.

[14] Y. Zhou, B. Zhou, L. Pache, M. Chang, A.H. Khodabakhshi, O. Tanaseichuk, C. Benner, S.K. Chanda, Metascape provides a biologist-oriented resource for the analysis of systems-level datasets, Nat. Commun. 10 (2019) 1523, https://doi.org/10.1038/s41467-019-09234-6.

[15] K.J. Livak, T.D. Schmittgen, Analysis of relative gene expression data using real-time quantitative PCR and the 2-ΔΔCT method, Methods 25 (2001) 402–408, https://doi.org/10.1006/meth.2001.1262.

[16] C. Branca, K. Khouzami, U. Wanderlingh, G. D'Angelo, Effect of intercalated chitosan/clay nanostructures on concentrated pluronic F127 solution: a FTIR-ATR, DSC and rheological study, J. Colloid Interface Sci. 517 (2018) 221–229, https://doi.org/10.1016/j.jcis.2018.02.004.

[17] I.R. Gibson, I. Rehman, S.M. Best, W. Bonfield, Characterization of the transformation from calcium-deficient apatite to β-tricalcium phosphate, J. Mater. Sci. Mater. Med. 11 (2000) 799–804, https://doi.org/10.1023/A:1008905613182.

[18] S.-H. Kwon, Y.-K. Jun, S.-H. Hong, H.-E. Kim, Synthesis and dissolution behavior of β-TCP and HA/β-TCP composite powders, J. Eur. Ceram. Soc. 23 (2003) 1039–1045, https://doi.org/10.1016/S0955-2219(02)00263-7.

[19] A. Saitoh, R.K. Brow, U. Hoppe, G. Tricot, S. Anan, H. Takebe, The structure and properties of xZnO–(67-x)SnO–P2O5 glasses: (I) optical and thermal properties, Raman and infrared spectroscopies, J. Non-Cryst. Solids 484 (2018) 132–138, https://doi.org/10.1016/j.jnoncrysol.2018.01.030.

[20] A. Sroka-Bartnicka, L. Borkowski, G. Ginalska, A. Ślósarczyk, S.G. Kazarian, Structural transformation of synthetic hydroxyapatite under simulated in vivo conditions studied with ATR-FTIR spectroscopic imaging, Spectrochim. Acta Mol. Biomol. Spectrosc. 171 (2017) 155–161, https://doi.org/10.1016/j.saa.2016.07.051.

[21] S. Batool, Z. Hussain, U. Liaqat, M. Sohail, Solid-state synthesis and process optimization of bone whitlockite, Ceram. Int. 48 (2022) 13850–13854, https://doi.org/10.1016/j.ceramint.2022.01.267.

[22] V.V. Kostov-Kytin, E. Dyulgerova, R. Ilieva, V. Petkova, Powder X-ray diffraction studies of hydroxyapatite and β-TCP mixtures processed by high energy dry milling, Ceram. Int. 44 (2018) 8664–8671, https://doi.org/10.1016/j.ceramint.2018.02.094.

[23] D. dos S. Tavares, L. de O. Castro, G.D. de A. Soares, G.G. Alves, J.M. Granjeiro, Synthesis and cytotoxicity evaluation of granular magnesium substituted β-tricalcium phosphate, J. Appl. Oral Sci. 21 (2013) 37–42, https://doi.org/10.1590/1678-7757201302138.

[24] N. Amirthalingam, T. Deivarajan, M. Paramasivam, Effect of heat treatment temperature on whitlockite prepared using Dolomite, Periodico 91 (2022), https://doi.org/10.37896/pd91.3/9134.

[25] N. Baek, O.W. Seo, J. Lee, J. Hulme, S.S.A. An, Real-time monitoring of cisplatin cytotoxicity on three-dimensional spheroid tumor cells, Drug Des Devel Ther 10 (2016) 2155–2165, https://doi.org/10.2147/DDDT.S108004.

[26] N. Baek, O.W. Seo, M. Kim, J. Hulme, S.S.A. An, Monitoring the effects of doxorubicin on 3D-spheroid tumor cells in real-time, OncoTargets Ther. 9 (2016) 7207–7218, https://doi.org/10.2147/OTT.S112566.

[27] E. Panczyszyn, V. Saverio, R. Monzani, M. Gagliardi, J. Petrovic, J. Stojkovska, L. Collavin, M. Corazzari, FSP1 is a predictive biomarker of osteosarcoma cells' susceptibility to ferroptotic cell death and a potential therapeutic target, Cell Death Discov. 10 (2024) 87, https://doi.org/10.1038/s41420-024-01854-2.

[28] F.E. Freeman, R. Burdis, O.R. Mahon, D.J. Kelly, N. Artzi, A spheroid model of early and late-stage osteosarcoma mimicking the divergent relationship between tumor elimination and bone regeneration, Adv Healthc Mater 11 (2022), https://doi.org/10.1002/adhm.202101296.

[29] M. Cortini, N. Baldini, S. Avnet, New advances in the study of bone tumors: a lesson from the 3D environment, Front. Physiol. 10 (2019), https://doi.org/10.3389/fphys.2019.00814.

[30] H. Chaddad, S. Kuchler-Bopp, G. Fuhrmann, H. Gegout, G. Ubeaud-Sequier, P. Schwinté, F. Bornert, N. Benkirane-Jessel, Y. Idoux-Gillet, Combining 2D angiogenesis and 3D osteosarcoma microtissues to improve vascularization, Exp. Cell Res. 360 (2017) 138–145, https://doi.org/10.1016/j.yexcr.2017.08.035.

[31] N.C. Negrini, C. Ricci, F. Bongiorni, L. Trombi, D. D'alessandro, S. Danti, S. Farè, An osteosarcoma model by 3D printed polyurethane scaffold and in vitro generated bone extracellular matrix, Cancers (Basel) 14 (2022), https://doi.org/10.3390/cancers14082003.

[32] C.F. Monteiro, S.C. Santos, C.A. Custódio, J.F. Mano, C.F. Monteiro, S.C. Santos, C. A. Custódio, J.F. Mano, Human platelet lysates-based hydrogels: a novel personalized 3D platform for spheroid invasion assessment, Adv. Sci. 7 (2020) 1902398, https://doi.org/10.1002/ADVS.201902398.

[33] C.F. Monteiro, C.A. Custódio, J.F. Mano, Bioengineering a humanized 3D tri-culture osteosarcoma model to assess tumor invasiveness and therapy response, Acta Biomater. 134 (2021) 204–214, https://doi.org/10.1016/j.actbio.2021.07.034.

[34] G. Bassi, S. Panseri, S.M. Dozio, M. Sandri, E. Campodoni, M. Dapporto, S. Sprio, A. Tampieri, M. Montesi, Scaffold-based 3D cellular models mimicking the heterogeneity of osteosarcoma stem cell niche, Sci. Rep. 10 (2020) 1–12, https://doi.org/10.1038/s41598-020-79448-y.

[35] M.F. Domingues, J.C. Silva, P. Sanjuan-Alberte, From spheroids to bioprinting: a literature review on biomanufacturing strategies of 3D in vitro osteosarcoma models, Adv. Ther. 7 (2024), https://doi.org/10.1002/adtp.202400047.

[36] J. Rodrigues, B. Sarmento, C.L. Pereira, Osteosarcoma tumor microenvironment: the key for the successful development of biologically relevant 3D in vitro models. https://doi.org/10.1007/s44164-022-00008-x, 2022.

[37] D.I. Petrescu, J.T. Yustein, A. Dasgupta, Preclinical models for the study of pediatric solid tumors: focus on bone sarcomas, Front. Oncol. 14 (2024), https://doi.org/10.3389/fonc.2024.1388484.

[38] S. Toosi, M.J. Javid-Naderi, A. Tamayol, M.H. Ebrahimzadeh, S. Yaghoubian, S. A. Mousavi Shaegh, Additively manufactured porous scaffolds by design for treatment of bone defects, Front. Bioeng. Biotechnol. 11 (2024), https://doi.org/10.3389/fbioe.2023.1252636.

[39] H.J. Haugen, S.P. Lyngstadaas, F. Rossi, G. Perale, Bone grafts: which is the ideal biomaterial? J. Clin. Periodontol. 46 (2019) 92–102, https://doi.org/10.1111/jcpe.13058.

[40] S. Samavedi, A.R. Whittington, A.S. Goldstein, Calcium phosphate ceramics in bone tissue engineering: a review of properties and their influence on cell behavior, Acta Biomater. 9 (2013) 8037–8045, https://doi.org/10.1016/j.actbio.2013.06.014.

[41] S.R. Rao, C.M. Edwards, J.R. Edwards, Modeling the human bone–tumor niche: reducing and replacing the need for animal data, JBMR Plus 4 (2020), https://doi.org/10.1002/jbm4.10356.

[42] L.K. Chim, A.G. Mikos, Biomechanical forces in tissue engineered tumor models, Curr Opin Biomed Eng 6 (2018) 42–50, https://doi.org/10.1016/j.cobme.2018.03.004.

[43] A. Micalet, E. Moeendarbary, U. Cheema, 3D *in vitro* models for investigating the role of stiffness in cancer invasion, ACS Biomater. Sci. Eng. 9 (2023) 3729–3741, https://doi.org/10.1021/acsbiomaterials.0c01530.

[44] I.L. Ivanovska, J.W. Shin, J. Swift, D.E. Discher, Stem cell mechanobiology: diverse lessons from bone marrow, Trends Cell Biol. 25 (2015) 523–532, https://doi.org/10.1016/j.tcb.2015.04.003.

[45] J. Hao, Y. Zhang, D. Jing, Y. Shen, G. Tang, S. Huang, Z. Zhao, Mechanobiology of mesenchymal stem cells: perspective into mechanical induction of MSC fate, Acta Biomater. 20 (2015) 1–9, https://doi.org/10.1016/j.actbio.2015.04.008.

[46] G. Lee, S.-B. Han, J.-H. Lee, H.-W. Kim, D.-H. Kim, Cancer mechanobiology: microenvironmental sensing and metastasis, ACS Biomater. Sci. Eng. 5 (2019) 3735–3752, https://doi.org/10.1021/acsbiomaterials.8b01230.

[47] A.K. Luu, A.M. Viloria-Petit, Targeting mechanotransduction in osteosarcoma: a comparative oncology perspective, Int. J. Mol. Sci. 21 (2020) 7595, https://doi.org/10.3390/ijms21207595.

[48] K. Kita, K. Asanuma, T. Okamoto, E. Kawamoto, K. Nakamura, T. Hagi, T. Nakamura, M. Shimaoka, A. Sudo, Cytoskeletal actin structure in osteosarcoma cells determines metastatic phenotype via regulating cell stiffness, migration, and transmigration, Curr. Issues Mol. Biol. 43 (2021) 1255–1266, https://doi.org/10.3390/cimb43030089.

[49] K.M. Charoen, B. Fallica, Y.L. Colson, M.H. Zaman, M.W. Grinstaff, Embedded multicellular spheroids as a biomimetic 3D cancer model for evaluating drug and drug-device combinations, Biomaterials 35 (2014) 2264–2271, https://doi.org/10.1016/j.biomaterials.2013.11.038.

[50] E. Jabbari, S.K. Sarvestani, L. Daneshian, S. Moeinzadeh, Optimum 3D matrix stiffness for maintenance of cancer stem cells is dependent on tissue origin of cancer cells, PLoS One 10 (2015) 1–21, https://doi.org/10.1371/journal.pone.0132377.

[51] T.R. Coughlin, A. Sana, K. Voss, A. Gadi, U. Basu-Roy, C.M. Curtin, A. Mansukhani, O.D. Kennedy, The effect of fluid flow shear stress and substrate stiffness on yes-associated protein (Yap) activity and osteogenesis in murine osteosarcoma cells, Cancers (Basel) 13 (2021), https://doi.org/10.3390/cancers13133128.

[52] E.F. Morgan, G.U. Unnikrisnan, A.I. Hussein, Bone mechanical properties in healthy and diseased states, Annu. Rev. Biomed. Eng. 20 (2018) 119–143, https://doi.org/10.1146/annurev-bioeng-062117-121139.

[53] J.H. Cole, M.C.H. van der Meulen, Whole bone mechanics and bone quality, Clin. Orthop. Relat. Res. 469 (2011) 2139–2149, https://doi.org/10.1007/s11999-011-1784-3.

[54] D.T. Reilly, A.H. Burstein, The mechanical properties of cortical bone, JBJS 56 (1974). https://journals.lww.com/jbjsjournal/fulltext/1974/56050/the_mechanical_properties_of_cortical_bone.12.aspx.

[55] C. Adamopoulos, A.N. Gargalionis, C. Piperi, A.G. Papavassiliou, Recent advances in mechanobiology of osteosarcoma, J. Cell. Biochem. 118 (2017) 232–236, https://doi.org/10.1002/jcb.25660.

[56] C.X. Wang, X. Zhou, M. Wang, Influence of sintering temperatures on hardness and Young's modulus of tricalcium phosphate bioceramic by nanoindentation technique, Mater Charact 52 (2004) 301–307, https://doi.org/10.1016/j.matchar.2004.06.007.

[57] A. Tricoteaux, E. Rguiti, D. Chicot, L. Boilet, M. Descamps, A. Leriche, J. Lesage, Influence of porosity on the mechanical properties of microporous β-TCP bioceramics by usual and instrumented Vickers microindentation, J. Eur. Ceram. Soc. 31 (2011) 1361–1369, https://doi.org/10.1016/j.jeurceramsoc.2011.02.005.

[58] F. Djouad, B. Delorme, M. Maurice, C. Bony, F. Apparailly, P. Louis-Plence, F. Canovas, P. Charbord, D. Noël, C. Jorgensen, Microenvironmental changes during differentiation of mesenchymal stem cells towards chondrocytes, Arthritis Res. Ther. 9 (2007) R33, https://doi.org/10.1186/ar2153.
[59] C.P. Blobel, ADAM19, in: Handbook of Proteolytic Enzymes, Elsevier, 2004, pp. 719–721, https://doi.org/10.1016/B978-0-12-079611-3.50218-4.
[60] Y. Zhu, X. Zhang, R. Gu, X. Liu, S. Wang, D. Xia, Z. Li, X. Lian, P. Zhang, Y. Liu, Y. Zhou, LAMA2 regulates the fate commitment of mesenchymal stem cells via hedgehog signaling, Stem Cell Res. Ther. 11 (2020) 135, https://doi.org/10.1186/s13287-020-01631-9.
[61] H. Su, Y. Yang, W. Lv, X. Li, B. Zhao, Bone marrow mesenchymal stem cell-derived exosomal microRNA-382 promotes osteogenesis in osteoblast via regulation of SLIT2, J. Orthop. Surg. Res. 18 (2023) 185, https://doi.org/10.1186/s13018-023-03667-y.
[62] W.-N. Xu, R.-Z. Yang, H.-L. Zheng, L.-S. Jiang, S.-D. Jiang, NDUFA4L2 regulated by HIF-1α promotes metastasis and epithelial–mesenchymal transition of osteosarcoma cells through inhibiting ROS production, Front. Cell Dev. Biol. 8 (2020), https://doi.org/10.3389/fcell.2020.515051.
[63] T.-Y. Kim, J.-K. Park, Y. Prasad Aryal, E.-S. Lee, S. Neupane, S. Sung, E. Pokharel, C.-Y. Yeon, J.-Y. Kim, J.-K. Jung, H. Yamamoto, C.-H. An, Y. Lee, W.-J. Sohn, I.-H. Jang, S.-Y. An, J.-Y. Kim, Facilitation of bone healing processes based on the developmental function of Meox2 in tooth loss lesion, Int. J. Mol. Sci. 21 (2020) 8701, https://doi.org/10.3390/ijms21228701.
[64] G. Yuan, S. Yang, Effect of regulator of G protein signaling proteins on bone, Front. Endocrinol. 13 (2022), https://doi.org/10.3389/fendo.2022.842421.
[65] C. Raynard, N. Tessier, A. Huna, M. Warnier, J.-M. Flaman, F. Van Coppenolle, S. Ducreux, N. Martin, D. Bernard, Expression of the calcium-binding protein CALB1 is induced and controls intracellular Ca2+ levels in senescent cells, Int. J. Mol. Sci. 23 (2022) 9376, https://doi.org/10.3390/ijms23169376.
[66] R. Subbarayan, D. Murugan Girija, S.T.K. Raja, A. Krishnamoorthy, D. Srinivasan, R. Shrestha, N. Srivastava, S. Ranga Rao, Conditioned medium-enriched umbilical cord mesenchymal stem cells: a potential therapeutic strategy for spinal cord injury, unveiling transcriptomic and secretomic insights, Mol. Biol. Rep. 51 (2024) 570, https://doi.org/10.1007/s11033-024-09503-8.
[67] L.L. Dunn, S. de Valence, J. Tille, P. Hammel, B.H. Walpoth, R. Stocker, B.A. Imhof, M. Miljkovic-Licina, Biodegradable and plasma-treated electrospun scaffolds coated with recombinant <scp>O</scp> lfactomedin-like 3 for accelerating wound healing and tissue regeneration, Wound Repair Regen. 24 (2016) 1030–1035, https://doi.org/10.1111/wrr.12485.
[68] X. Li, P. Liu, W. Liu, P. Maye, J. Zhang, Y. Zhang, M. Hurley, C. Guo, A. Boskey, L. Sun, S.E. Harris, D.W. Rowe, H.Z. Ke, D. Wu, Dkk2 has a role in terminal osteoblast differentiation and mineralized matrix formation, Nat. Genet. 37 (2005) 945–952, https://doi.org/10.1038/ng1614.
[69] G. Yang, B. Mahadik, J.Y. Choi, J.P. Fisher, Vascularization in tissue engineering: fundamentals and state-of-art, Prog. Biomed. Eng. 2 (2020) 012002, https://doi.org/10.1088/2516-1091/ab5637.
[70] F. Simunovic, G. Finkenzeller, Vascularization strategies in bone tissue engineering, Cells 10 (2021) 1749, https://doi.org/10.3390/cells10071749.
[71] R.S. Kerbel, Tumor angiogenesis, N. Engl. J. Med. 358 (2008) 2039–2049, https://doi.org/10.1056/NEJMra0706596.
[72] R. Zamborsky, M. Kokavec, S. Harsanyi, L. Danisovic, Identification of prognostic and predictive osteosarcoma biomarkers, Medical Sciences 7 (2019) 28, https://doi.org/10.3390/MEDSCI7020028, 2019, Vol. 7, Page 28.
[73] W. Ren, G. Gu, Prognostic implications of RB1 tumour suppressor gene alterations in the clinical outcome of human osteosarcoma: a meta-analysis, Eur. J. Cancer Care 26 (2017) e12401, https://doi.org/10.1111/ECC.12401.
[74] J. Wiltfang, H.A. Merten, K.A. Schlegel, S. Schultze-Mosgau, F.R. Kloss, S. Rupprecht, P. Kessler, Degradation characteristics of α and β tri-calcium-phosphate (TCP) in minipigs, J. Biomed. Mater. Res. 63 (2002) 115–121, https://doi.org/10.1002/jbm.10084.
[75] S.P. Yu, Regulation and critical role of potassium homeostasis in apoptosis, Prog Neurobiol 70 (2003) 363–386, https://doi.org/10.1016/S0301-0082(03)00090-X.
[76] J. Iorio, G. Petroni, C. Duranti, E. Lastraioli, Potassium and sodium channels and the Warburg effect: biophysical regulation of cancer metabolism, Bioelectricity 1 (2019) 188–200, https://doi.org/10.1089/bioe.2019.0017.
[77] A. Romani, Regulation of magnesium homeostasis and transport in mammalian cells, Arch. Biochem. Biophys. 458 (2007) 90–102, https://doi.org/10.1016/j.abb.2006.07.012.
[78] A.M.P. Romani, Cellular magnesium homeostasis, Arch. Biochem. Biophys. 512 (2011) 1–23, https://doi.org/10.1016/j.abb.2011.05.010.
[79] E.C. Novosel, C. Kleinhans, P.J. Kluger, Vascularization is the key challenge in tissue engineering, Adv. Drug Deliv. Rev. 63 (2011) 300–311, https://doi.org/10.1016/j.addr.2011.03.004.
[80] T. Kaully, K. Kaufman-Francis, A. Lesman, S. Levenberg, Vascularization—the conduit to viable engineered tissues, Tissue Eng Part B Rev 15 (2009) 159–169, https://doi.org/10.1089/ten.teb.2008.0193.
[81] J. Stalin, B.A. Imhof, O. Coquoz, R. Jeitziner, P. Hammel, T.A. McKee, S. Jemelin, M. Poittevin, M. Pocard, T. Matthes, R. Kaci, M. Delorenzi, C. Rüegg, M. Miljkovic-Licina, Targeting OLFML3 in colorectal cancer suppresses tumor growth and angiogenesis, and increases the efficacy of anti-PD1 based immunotherapy, Cancers (Basel) 13 (2021) 4625, https://doi.org/10.3390/cancers13184625.
[82] R. Burgos-Panadero, F. Lucantoni, E. Gamero-Sandemetrio, L. de la Cruz-Merino, T. Álvaro, R. Noguera, The tumour microenvironment as an integrated framework to understand cancer biology, Cancer Lett. 461 (2019) 112–122, https://doi.org/10.1016/j.canlet.2019.07.010.
[83] M. Baxter-Holland, C.R. Dass, Doxorubicin, mesenchymal stem cell toxicity and antitumour activity: implications for clinical use, J. Pharm. Pharmacol. 70 (2018) 320–327, https://doi.org/10.1111/jphp.12869.
[84] M. Cortini, F. Macchi, F. Reggiani, E. Vitale, M.V. Lipreri, F. Perut, A. Ciarrocchi, N. Baldini, S. Avnet, Endogenous extracellular matrix regulates the response of osteosarcoma 3D spheroids to doxorubicin, Cancers (Basel) 15 (2023) 1221, https://doi.org/10.3390/cancers15041221.
[85] R.K. Jain, J.D. Martin, T. Stylianopoulos, The role of mechanical forces in tumor growth and therapy, Annu. Rev. Biomed. Eng. 16 (2014) 321–346, https://doi.org/10.1146/annurev-bioeng-071813-105259.
[86] T. Stylianopoulos, The solid mechanics of cancer and strategies for improved therapy, J. Biomech. Eng. 139 (2017), https://doi.org/10.1115/1.4034991.